Processing a non-weldable nickel-base superalloy by Selective Laser Melting: role of the shape and size of the melt pools on solidification cracking

D. Grange, Jean-Dominique Bartout, B. Macquaire, C. Colin

Version of Record: https://www.sciencedirect.com/science/article/pii/S2589152920301034
Manuscript_b374b8b672b10aa852a0708ad18a9c20

Processing a non-weldable Nickel-base superalloy by Selective Laser Melting: role of the shape and size of the melt pools on solidification cracking

D. Grange[a,b*], J-D. Bartout[a], B. Macquaire[b], C. Colin[a]

[a]MINES ParisTech, PSL Research University, MAT – Centre des matériaux, CNRS UMR 7633, BP 87 91003 Evry, France

[b]Safran Additive Manufacturing, a technology platform of Safran Tech, Rue des Jeunes Bois, Châteaufort, 78114 Magny-Les-Hameaux, France

Abstract

The use of laser-based additive manufacturing for the fabrication of parts exposed to very high temperature in the aerospace and energy sectors is still very limited. Indeed, non-weldable superalloys tend to crack during their processing by Selective Laser Melting (SLM). Inconel 738 LC processed by SLM is subjected to solidification cracking. In this study, attention is focused on the influence of size and shape of the melt pools involved in the fabrication on the occurrence of cracking. This approach is motivated by the fact that the size and shape of the melt pools greatly affect the solidification conditions. Samples were fabricated with various

* Corresponding author at *MINES ParisTech, Centre des matériaux, 91003 Evry, France*. Tel.: (+33) 6 37 30 74 54; Email address: david.grange@mines-paristech.fr

fabrication parameters, leading to different melt pool sizes and shapes and different cracking intensity. It is shown that the cracking is minimal when the fabrication uses narrow melt pools and a strong overlap between adjacent melt pools. These observations were discussed in the light of solidification theory. As the cracks are known to appear primarily at high-angle grain boundaries, the effect of grain structure is investigated. These observations allowed the fabrication of a dense and crack-free material.

Keywords: Selective laser melting (SLM), Nickel-base superalloy, IN738LC, Solidification cracking, Melt pool

---

1. Introduction

Shaping hard metals with a laser beam is a complicated exercise. For years, precipitation hardening of nickel-base superalloys has been widely used in aerospace and energy sectors for the fabrication of parts with an exceptional high-temperature strength. Although these materials were initially designed for casting, there is today a strong industrial interest in being able to shape them with the Selective Laser Melting (SLM) process. A reinforcement of the γ matrix by a volume fraction of γ'-Ni_3(Al, Ti) precipitates between 40% and 80% is necessary for high-temperature properties [1,2], but this reinforcement unfortunately also increases the susceptibility of the materials to cracking during either their melting by a laser source or during further heat-treatments. Welding literature describes a typology of cracks that includes solidification cracking, ductility dip, liquation or strain age cracking [3–6]. There is today active research on the best way to fabricate defect-free parts using laser-based additive manufacturing processes.

In previous studies, microscopic solidification cracks were observed on samples produced by SLM with different alloys: IN738LC [7,8], CM247 LC [9] and Hastelloy X [10,11]. Even if this study focuses on solidification cracking, it can be mentioned that cracking during heat-treatment was also observed for Inconel 738 LC [13] and CM247 LC [14] processed by SLM. Solidification cracks are problematical: only the ones located in the bulk of the material can be healed with a hot isostatic pressing (HIP) treatment, whereas surface cracks will remain open. Kunz, Etter, Grässlin and Shklover [12] reported that they were able to produce samples in IN738LC for mechanical tests without cracks, with a HIP treatment. It was possible because

the specimens were machined and thus the surface cracks were removed. Nevertheless, the scaled-up production of net shape parts with that solution is not possible.

A first possible solution to prevent solidification cracking is to control or modify the alloy composition. Several authors focused on the role of minor elements in various alloys. Engeli, Etter, Hövel and Wegener [7] processed by SLM with the same fabrication parameters eight batches with different compositions in the specification range of Inconel 738 LC. They calculated the correlation between the crack density and the composition in thirty-one minor elements. They concluded that there is a strong detrimental effect of elements Si and Pb. Cloots, Uggowitzer and Wegener [8] measured the segregation profile of minor elements at grain boundaries after solidification and suggest an effect of Zr and B on cracking susceptibility. Tomus, Rometsch, Heilmaier and Wu [10] proposed that Si, Mn and C have a strong influence on solidification cracking of Hastelloy X. Chauvet et al. [15] observed the presence of phases rich in B at grain boundaries with a superalloy (Ti + Al=8.6 wt%) processed by Electron Beam Melting (EBM) and concluded in an important role of these phases. At this point, there is a general agreement on an effect of minor elements, but conclusions sometimes differ when it comes to ranking the effect of the different elements. Moreover, several authors underline that some minor elements (B and C) are useful for high temperature mechanical properties.

A second possible solution is an optimization of the fabrication parameters. Some studies investigate the effect of the fabrication parameters on solidification cracking. Carter, Attallah and Reed [9] noted a decrease in the cracking density of samples in CM247 LC when the scanning velocity of the laser beam was increased. They also observed an ambiguous role of

the hatching space, which is the distance between two scanning tracks. Depending on the other fabrication parameters, an increase of the hatching space resulted either in more cracks or less cracks. In the same way, Cloots et al. [8] observed with a fixed laser power ($P = 200W$) and a fixed hatching space that an increase of the scanning speed resulted in less cracks but also more porosity. He concluded that there is a necessary compromise between suppressing microcracking and having a dense material. To optimize the fabrication with the SLM process, it is worth remembering that the interaction of the laser beam with the powder bed creates a pool of liquid metal (melt pool), whose geometry depends very strongly on the fabrication parameters. This geometry is very important because it determines the solidification conditions [16] (solidification gradient G and solidification velocity v_S) at the origin of microstructures and defects as pores and solidification cracks. So far, no study has focused on the link between the shape or size of the melt pool and the microcracking phenomena. The objective of the present work is to elucidate the link between the process parameters, the geometry or size of melt pools and the occurrence of the defects. The main finding is that it is possible to simultaneously avoid cracks and obtain a dense material, by a control of the melt pool size combined with a control of the overlap between melt pools. The effect of the grain structure and of the mechanical stresses were also investigated.

2. Experiments

2.1. Processing conditions

To highlight a link between the melt pool shape and the crack density, samples were built in a large space of processing parameters. The objective is to find correlations between the melt

pool dimensions and the crack density, before investigating the physical reasons. For the fabrication of the specimens, a gas-atomized IN738LC powder was used with a composition given in Table 1. The composition was measured by Inductively Coupled Plasma (ICP) for Cr, Co, Mo, W, Nb, Ta, Ti and Al, by ICP / Mass spectrometry (MS) for B, Cu, Fe, Si and Zr and by LECO combustion for C. The particle size distribution is gaussian, with diameter percentiles $D_{10} = 17\mu m$, $D_{50} = 28\mu m$, $D_{90} = 45\mu m$. The specimens are 10mm cubes, fabricated using a Concept Laser M2 machine. They were built on a plate in IN625 on a 2mm height of lattice supports in order to facilitate cutting after fabrication. All the samples have in common the following fabrication parameters: a layer thickness $\Delta Z = 40\mu m$, a laser beam $1/e^2$ diameter $\phi_L =$ 100µm and a bidirectional scanning pattern with a rotation of 90° of scanning direction between each layer (Figure 1.a). This scanning pattern was chosen to facilitate observation of the melt pools. The variable parameters are the laser power P (85 – 370W), the scanning speed v_L (380 – 1600mm/s) and the hatching space h_s (75 - 195μm). We generated a near random sample of 40 parameters using Latin hypercube sampling. To avoid unnecessary work with an unsuccessful building of samples or with a fabrication interruption, we selected a region of interest based on previous experience. First, only the parameters with a ratio P/v_L between 0.15 and 0.7 J/mm were retained. Thanks to an estimation of the melt pool width coming from a previous work, only the parameters for which the estimated overlap ratio between adjacent melt pools (see definition in section 3.2) was positive and under 0.6 were retained. This led to the selection of 14 points, to which 9 parameters were added for a repetition of (P, v_L) couples for different values of the hatching space h_S. In total, sample were built with

23 different parameters. Figure 1.b represents graphically the value of the fabrication parameters in a coordinate reference $(v_L/v_L^{max}, P/P^{max})$, and in a reference (E_l, h_S), where E_l = P / v_L is the linear incident energy on the powder bed. The dots noted with squares, triangles or stars correspond to pairs (P, v_L) that have been used with several values of the hatching space.

On the graph on the right, an increase in hatching space as a function of the linear energy is visible. It results from the selection explained above and will be discussed further in the article.

Cr	Ni	Co	Mo	W	Nb	Ta	Ti	Al	B	C	Fe	Si	Cu	Zr
16.1	Bal	8.82	1.78	2.61	0.85	1.75	3.37	3.46	0.01	0.10	0.05	0.048	0.001	0.063

Table 1 – Weight composition in percent of Inconel 738 LC.

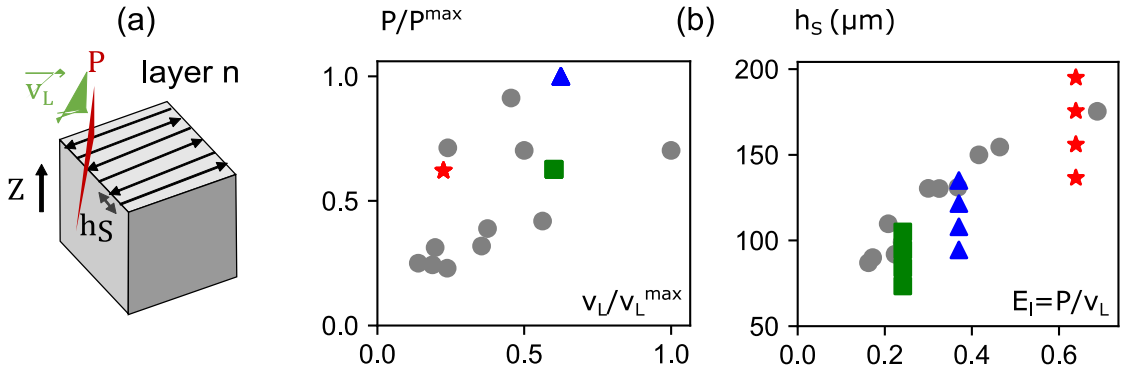

Figure 1 – Fabrication parameters : (a) schematic representation of primary process parameters ; (b) values of parameters used in this work.

2.2. Crack observation and melt pool observation

The nature of the cracks was identified on the sample with $E_l = 0.24J/mm$ and $h_S = 105\mu m$. After a midplane cut, Electron Back Scattered Diffraction (EBSD) was performed in a FEI Nova NanoSEM 450 with an EDAX Hikari EBSD camera. The acceleration tension was 20kV and the probe current was 10nA. An EBSD map of size 325 x 950 μm was taken at the center

of the top of the sample with a 1µm step size. The data was analyzed using the OIM Analysis™ v7 software. The crack surface was examined after bending the sample up to failure. Was used for observation, a Zeiss Gemini Sigma 300 Scanning Electron Microscope (SEM) with an Everhart-Thornley secondary electron (SE) detector and an acceleration tension of 5kV. The shape of the melt pools was revealed with a Glycerigia etching (15 ml HCl + 10 ml glycerol + 5 ml HNO_3, 20s by swabbing) followed by an observation with an optical microscope.

2.1. Crack quantitative analysis and microstructure observation

For a quantitative analysis of cracks with the best statistical reliability, a cartography of the whole 10mm x 10mm midplane section of each cube was performed with a Keyens optical microscope. A polishing down to $0.04\mu m$ colloidal silica finish enabled the detection of thin ($1\mu m$ wide) cracks and a good contrast necessary for image analysis. A processing with the software ImageJ allowed to distinguish the different types of defects (cracks and pores), with meticulous visual verification after the processing of every image. As a result, a crack density, that is to say a cumulative length of cracks per unit area (in mm/mm²), was calculated for every sample. In the same way, a fraction area of pores was evaluated. Microstructure observation was performed with a Zeiss Gemini Sigma 300 SEM and with an In-Lens secondary electron detector, after a Glycerigia etching.

3. Results

3.1. Solidification cracking

Microscopic cracks are visible on Figure 2.a: they measure typically $100\mu m$ and are mainly vertical and located at grain boundaries. The crack surface was observed after bending the

sample up to failure, see Figure 2.b. Dendritic microstructures are visible on the fracture surface. This is a sign of the presence of residual interdendritic liquid when the crack was formed. As other authors have concluded, this material processed by SLM is subjected to solidification cracking [7,8,17]. Other crack surfaces in the sample also show the dendritic structure, with nanoporosity visible between the dendrite arms (Figure 2.c). This demonstrates a lack of liquid metal feeding in the last stages of solidification, causing a poor cohesion between dendrites.

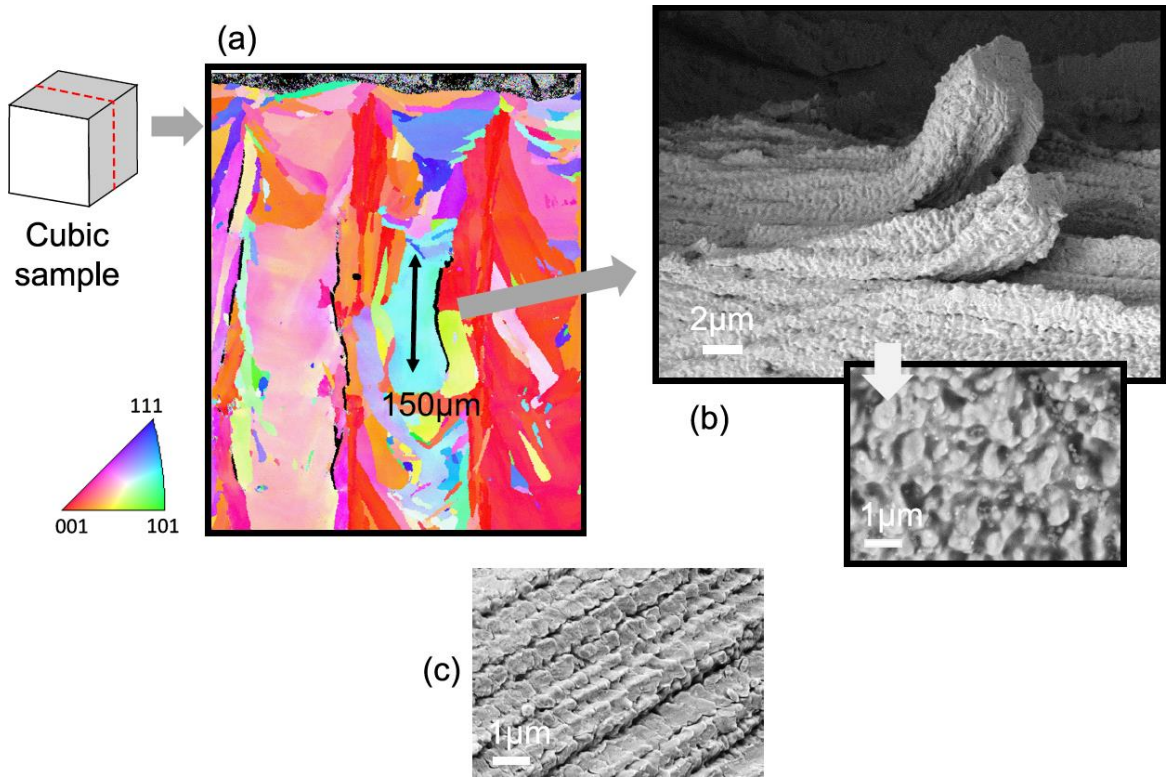

Figure 2 - Solidification cracking of an Inconel 738 sample processed by SLM: (a) microscopic vertical cracks located at grain boundaries, (b) dendritic microstructure visible on the crack surface, sign of residual liquid during the cracking, (c) nanoporosity between the dendrite arms visible on another crack surface of the sample.

3.2. Melt pool shape and size

Figure 3.a shows the melt pools observable with the optical microscope after etching. The fabrication pattern is well visible on the image. Because of the 90° rotation of the scanning speed vector $\overrightarrow{v_L}$ between two fabrication layers, the transversal cross section of the sample

shows transversal sections of the melt pools in a layer and longitudinal sections in the next layer. A crack is visible: it initiates in a layer, transversally to a melt pool, and then propagates in several higher layers. As explained before, the objective of this study is to link the occurrence of these defects within the melt pool geometry on a large set of fabrication parameters. For that purpose, some characteristic dimensions of the melt pools (Figure 3.b) are measured in the top layer of the sample: the melt pool width W_{MP} and the height of the remelting zone H_{RZ}. Measures are taken on ten adjacent melt pools in the center of the sample. Let us note that a melt pool is never fully visible as it has been partially remelted by the following one. As a consequence, the half width on the left-side of the melt pool, which is always visible, was measured. Figure 3.c shows the evolution of W_{MP} and H_{RZ} with respect to the linear energy $E_l = P/v_L$ (J/mm) and to the hatching space h_S. In SLM process as in welding, it is common knowledge that melt pool size increases with respect to linear energy [18], up to the *keyhole* regime (vaporization), which is inappropriate for SLM because it causes porosity in the material (see section 3.4). An effect of the hatching space on the melt pool dimensions was also observed, especially for high energy fabrication parameters ($E_l > 0.3J/mm$). The overlap ratio τ_R depends both on W_{MP} and h_S:

$$\tau_R = 1 - \frac{h_S}{W_{MP}} \qquad \text{Equation 1}$$

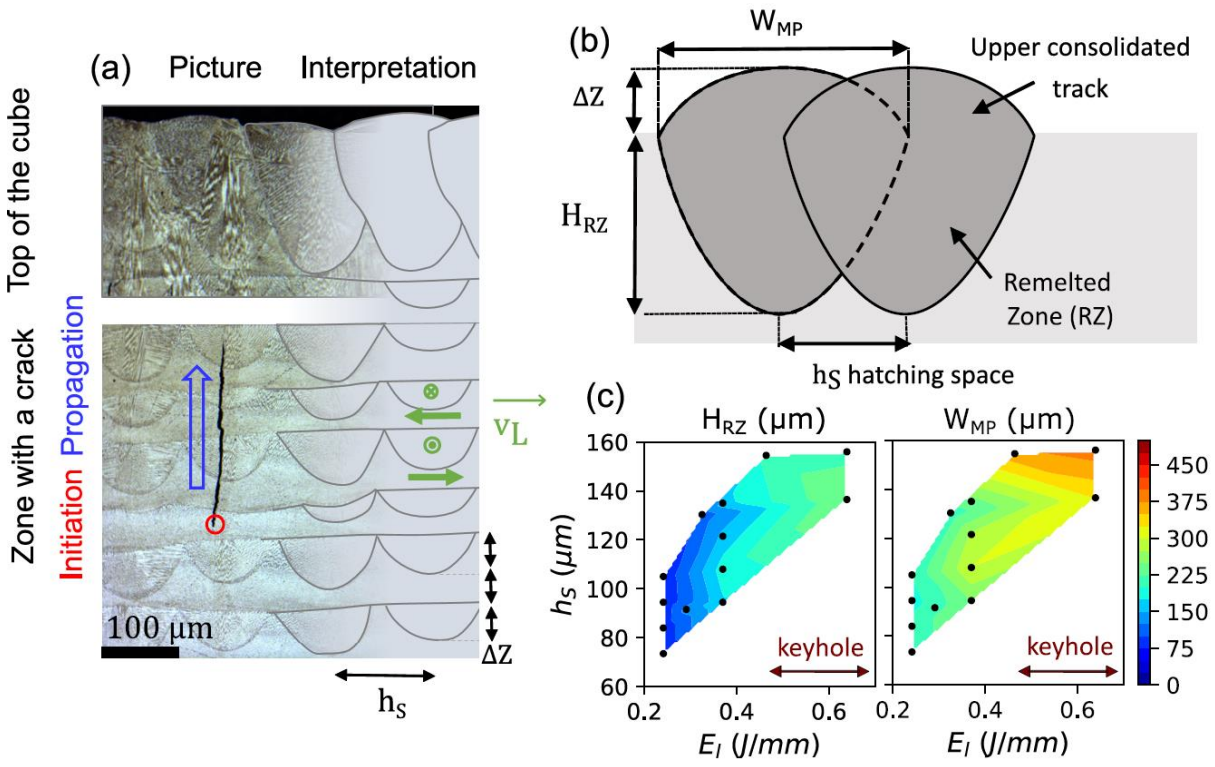

Figure 3 – (a) Initiation of a solidification crack transversally to the melt pool and propagation in higher layers ; (b) Some geometrical features of melt pools ; (c) Melt pool width W_{MP} and remelted zone height H_{RZ} as a function of linear energy $E_l = P/v_L$ and hatching space h_S.

3.3. Cracking density

The samples exhibit a very wide range of crack density: the most heavily cracked sample has a density of 3.5mm/mm² whereas the best sample is 18 times less cracked (0.2mm/mm²) and only features a few cracks on its sides. It confirms the very strong influence of fabrication parameters on cracking. Correlations between the crack density and criteria based on the process parameters ($P, v_L, h_S, E_l,\ E_V = P/(v_L.h_S.\Delta Z)$[1]) or based on the dimensions of the melt pools ($W_{MP}, H_{RZ},\ H_{RZ}/W_{MP}$) were investigated. The determination coefficients R^2 of the linear regressions between the output variable (crack density) and the different variables cited above

[1] This criterion corresponds to a volumetric energy density (J/mm^3), often used in the SLM process [19,20].

were calculated, see Table 2.

	P (W)	v_L (mm/s)	h_S (mm)	E_l (J/mm)	E_V (J/mm^3)	W_{MP} (mm)	H_{RZ} (mm)	H_{RZ}/W_{MP}
a	1.79e-3	-1.26e-3	2.38e+1	4.51	2.49e-2	6.22	6.36	1.61
b	1.10	2.39	-1.41	-1.69	-3.22e-1	-1.04e-1	5.62e-1	1.56e-1
R^2	0.03	0.24	0.75	0.69	0.26	0.33	0.29	0.12

Table 2 – Value of the slope a, the intercept b and the determination coefficient R^2 of linear regressions between the crack density different explanatory variables.

The best correlation found (i.e. higher R^2) is between the crack density and the hatching space h_S, which is presented on Figure 4. The lesser the hatching space, the fewer cracks. To interpret this correlation, it is recalled that:

$$h_S = \overset{(1)}{W_{MP}} \times \overset{(2)}{(1-\tau_R)}, \qquad \text{Equation 2}$$

where τ_R is the overlap ratio defined in Equation 1. This let us note two contributions for this trend:

1) *Effect of the melt pool width* W_{MP}: the density of cracks decreases when the melt pools are narrower (W_{MP} is smaller). Given the result of Figure 3.c, this is equivalent to saying that the density of cracks decreases when the linear energy E_l decreases. On Figure 4, the red dots (stars) correspond to a superior linear energy (0.64J/mm) than the green dots (squares) and their crack density is about three times higher. Let us note however that the determination coefficient of the correlation between the crack density and the melt pool width W_{MP} is only $R^2 = 0.33$, which means that the melt pool width does not fully explain the crack density.

2) *Effect of the overlap*: at equal melt pool size, the crack density drops when the overlap

between the melt pools rises. For example, the green dots (squares) all have a linear energy of 0.24J /mm and width $W_{MP} = 200 \pm 10\mu m$. Among these points, a higher overlap ratio τ_R (i.e. a smaller hatching space h_S) leads to less cracking. The same trend is valid for blue dots (triangles) and red dots (stars).

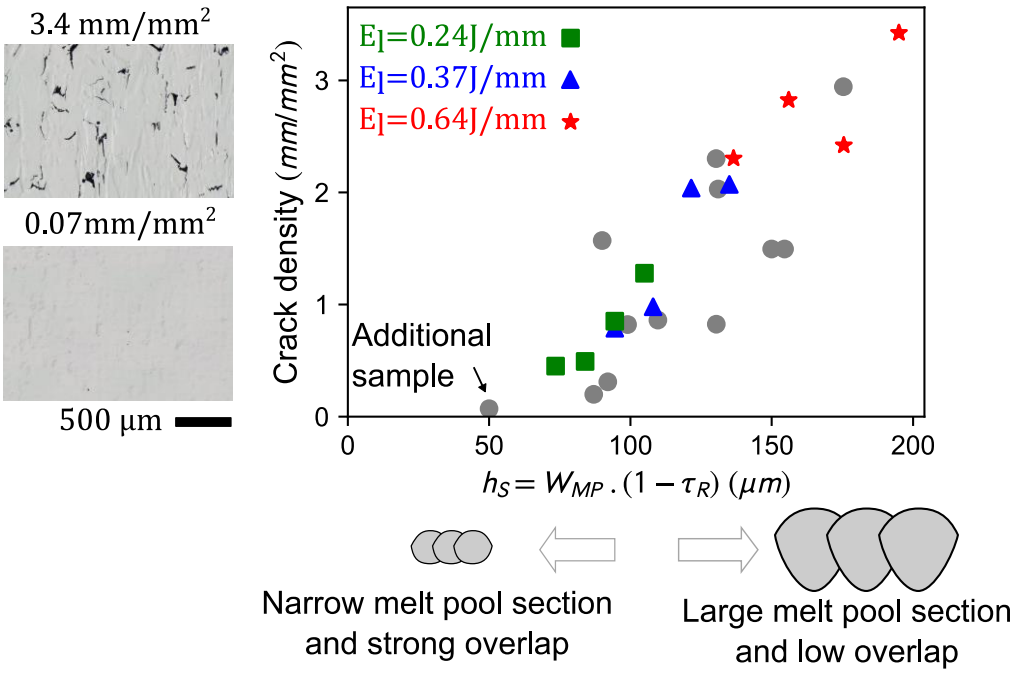

Figure 4 - Effect of fabrication parameters on the crack density.

Following this finding, an additional sample was fabricated with a very low linear energy ($E_l = 0.09 J/mm$) and a very low hatching space. As expected, it features the lowest crack density: 0.07mm/mm², with only a few cracks located close to the free faces of the cube.

3.4. Porosity

The observation with the optical microscope revealed different types of pores. First, round pores were observed for high linear energies ($E_l > 0.45 J/mm$). They are typical of keyhole porosity, caused by the vaporization of the metal [21]. Second, lack of fusion porosity in some samples resulted from an insufficient overlap between adjacent melt pools, so that some amount of

powder remained unmelted between them [20]. Considering a fixed hatching space, this occurs when the linear energy is too low. Porosity can then be reduced either by increasing the linear energy or by decreasing the hatching space. Finally, irregularities of the upper surface of the cubes occurred either at high scanning velocities ($v_L > 1600mm/s$) due to the humping phenomenon [22] or for combined conditions of low linear energy and low power ($E_l < 0.22J/mm$ and $P < 100W$) due to capillary instabilites [23]. These irregularities led to an inhomogeneous powder bed thickness, so that the powder bed in some locations was too thick to be fully melted by the laser beam. An example of pores resulting from keyhole regime and lack of fusion are visible on Figure 5.a. Figure 5.b represents the surface fraction of pores as a function of the overlap ratio, for the samples that were not affected by keyhole porosity or by upper surface irregularities. One can see that a relative density over 99.9% is achievable by using an overlap ratio over 0.4. Given Equation 1, the values of the hatching space h_S suitable for the fabrication increase with E_l, as shown in Figure 1. Cloots et al. [8] concluded in their study that "since porosity and crack density exhibit and inverse relationship, a trade-off in the choice of the process parameters to process IN738LC with SLM is necessary". On the contrary, it was possible in this work to produce a sample with both a low cracking density and a low porosity. This is possible by decreasing not only P/v_L, but also the hatching space h_S in parallel (see Figure 1.b), to obtain a sufficient overlap ($\tau_R = 40\%$) and thus a low porosity. For example, the additional sample which features the minimal microcracking density also has a relative density over 99.9%.

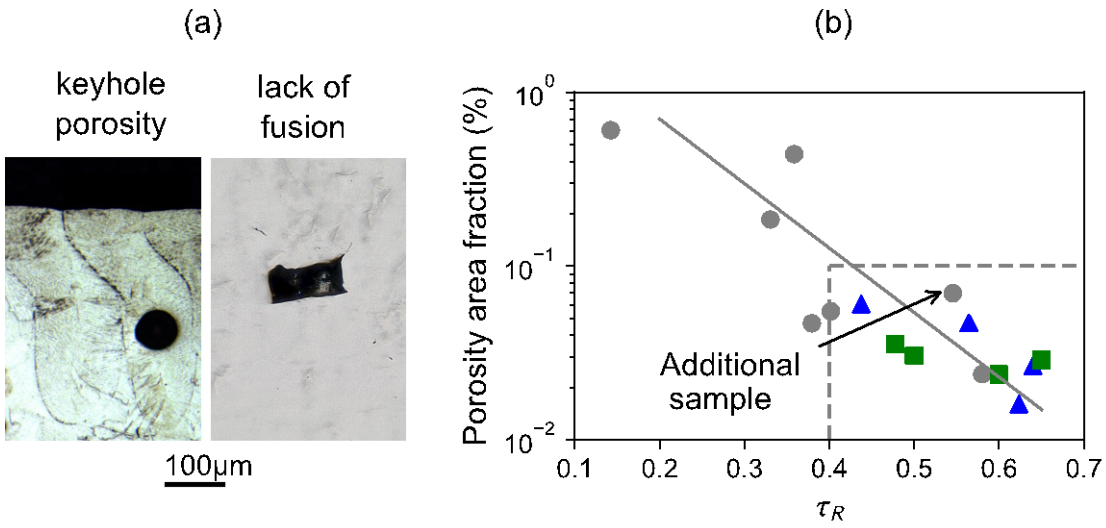

Figure 5 – (a) Keyhole porosity and lack of fusion porosity on samples; (b) Relation between the overlap ratio and the surface fraction of pores. The samples affected by keyhole or humping phenomenon are not represented on the graph.

3.5. Microstructure

The as-built specimens exhibit a very thin microstructure (Figure 6), with a primary dendrite arm spacing (PDAS) of an order of magnitude of $\lambda_1 \sim 600nm$ and TiC carbides in interdendritic regions with a size inferior to 200nm, as observed in Ref. [24]. Despite a composition rich in γ'-forming elements (Al+Ti+Ta+Nb >13% at), potential γ' precipitates are too small to be visible with a 50 000 magnification and the In-Lens detector.

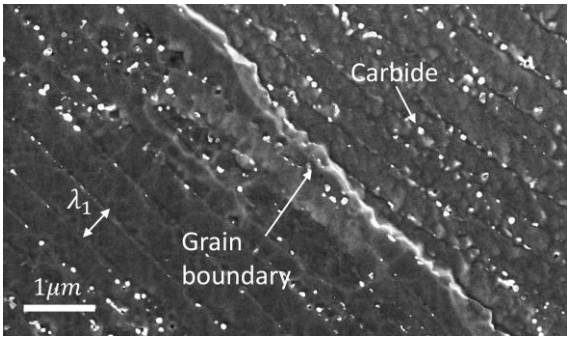

Figure 6 - Microstructure on one of the samples (0.24J/mm) observed with a SEM In Lens SE Detector.

4. Discussion

4.1. Solidification cracking mechanism

In casting and welding processes, solidification is known to occur under two necessary conditions: mechanical stresses in the mushy zone and insufficient liquid feeding in a brittle temperature range (BTR), at the end of solidification (see Figure 7), between two characteristic values of solid fraction f_s. In the corresponding temperature range, the solid dendritic network is coherent [25], allowing mechanical stresses to be transmitted . A tensile stress between grains can still separate them, because a liquid film between them remains. If the available liquid pressure is not high enough, the separation causes a rupture of the liquid film and then a crack to appear. Despite the general agreement that the brittle temperature range is close to the end of solidification, the critical values of f_s differ between authors. For example, Clyne and David suggested that the alloy is brittle when f_s is comprised between 0.9 and 0.99 [26].

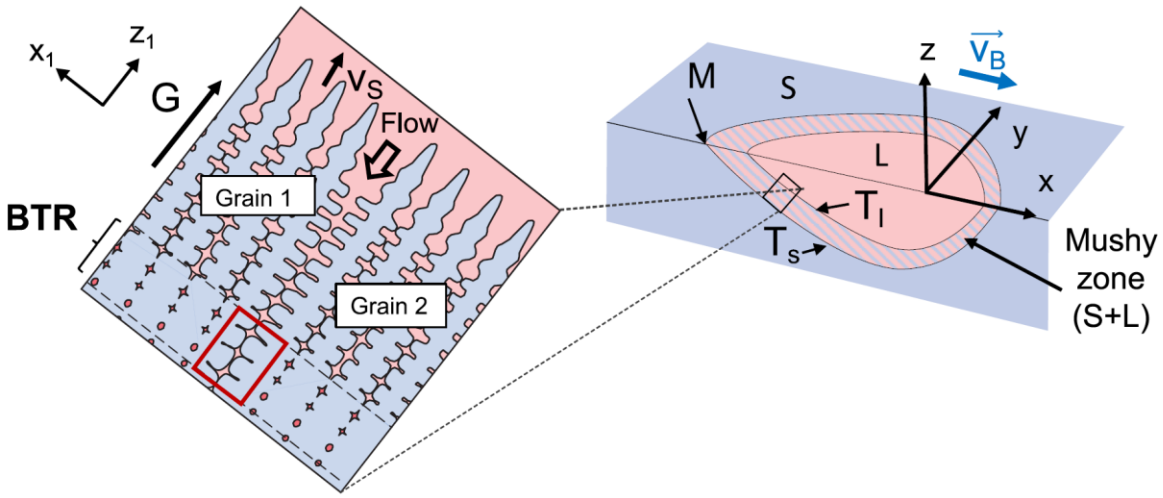

Figure 7 - Solidification cracking mechanism, adapted from Dantzig and Rappaz [25] : T_l is the liquidus temperature, T_s the solidus temperature and v_s the liquidus isotherm velocity.

Rappaz, Drezet and Gremaud [27] proposed a model for solidification cracking ("RDG model",

based on the pressure drop of the liquid phase in the mushy zone. If the pressure drop Δp_l exceeds a critical value, a crack will initiate. They suggest the following expression of Δp_l:

$$\Delta p_l = \Delta p_l^{\epsilon_s} + \Delta p_l^{\beta} = (1+\beta)\mu_l \int_0^L \frac{\dot{E}(z_1)}{K} dz_1 + v_S \beta \mu_l \int_0^L \frac{g_l}{K} dz_1 \qquad \text{Equation 3}$$

where β is the solidification shrinkage, μ_l is the viscosity of the liquid phase, L is the extent of the mushy zone (i.e. the distance between the dendrite root at $z_1 = 0$ and dendrite tip at $z_1 = L$), $\dot{E}$ is the cumulative average deformation rate of the solid, defined as $\dot{E} = \int_0^{z_1} g_s \dot{\epsilon}_{s,x_1x_1}(z_1) dz_1$, g_s and g_l are the volume fraction of solid and liquid, $\dot{\epsilon}_{s,x_1x_1}$ is the strain rate in the solid, K is the permeability of the mushy zone, v_T is the isotherm velocity. This model highlights both contributions for solidification cracking: the strain in the mushy zone (term $\Delta p_l^{\epsilon_s}$) and the lack of liquid metal feeding (term Δp_l^{β}). Let us mention that both terms increase with the extent of the mushy zone L. The estimation of the full expression of the pressure drop would require a calculation of the strains in the mushy zone, which is not the scope of this article. Nevertheless, we discuss in the following subsections the effect of the extent of the mushy and the effect of mechanical stresses.

4.2. Extent of the mushy zone

As most solidification cracking criteria, RDG model describes that a large mushy zone is more likely to cause cracking. The extent of the mushy zone L has an influence on both terms $\Delta p_l^{\epsilon_s}$ and Δp_l^{β}. In this study, it is interesting to explore a possible effect of the extent of the mushy zone on the crack density. The effect of the processing parameters on the extent of the mushy zone can be estimated with Rosenthal model [28]. Due to the simplicity of this model, the results are expected to be mainly qualitative, as more complex models including liquid convection are

necessary to reflect correctly the melt pool shape in high-energy conditions. According to Rosenthal model, the thermal field $T(x,y,z)$ around a punctual laser source is:

$$T - T_{sub} = \frac{A.P}{2\pi kr}\exp\left(-\frac{v_L(r+x)}{2\alpha}\right) \quad \text{Equation 4}$$

where T_{sub} is the substrate temperature far from the melt pool, A the absorption coefficient, $r = \sqrt{x^2+y^2+z^2}$, k the material thermal conductivity and α the material thermal diffusivity. These properties were estimated at solidus temperature from measurements by Quested et al. [29]: $\alpha = 4.10^{-6}m^2s^{-1}$, $k = 25Wm^{-1}K^{-1}$. For the solidus and liquidus temperatures, the Thermocalc software was used with TCNI9 database. As in other studies [8,10,15,17], it was considered that Gulliver-Scheil model (i.e. infinite diffusion of chemical species in the liquid phase and no diffusion in the solid phase) is the best model available to describe rapid non-equilibrium solidification, although it does not account for possible solute trapping [30,31]. No phase was rejected in the calculation and the solidus temperature was assimilated to the temperature when the mass solid fraction is 0.99. These assumptions resulted in a liquidus temperature $T_l = 1340°C$ and a solidus temperature $T_s = 1027°C$. Note that liquidus temperature is quite close to the one measured by Quested et al. by differential scanning calorimetry (DSC) at 10K/min (1355°C), whereas the solidus temperature is significantly lower than the one measured by DSC (1239°C), which is consistent with the non-equilibrium Scheil solidification. An absorption coefficient of 0.7 was chosen, so that the depth the solidus isotherm matches $H_{RZ} = 78\mu m$ for the case $E_l = 0.24J/mm$. Figure 8.a shows the temperature field on a longitudinal cut (x, 0, z) of the melt pool, with Rosenthal model. The liquidus and solidus isotherm are represented as black lines: melting occurs on the right and

solidification on the left. The extent of the mushy zone $L(x)$ is the distance between the two isotherms: it is plotted as a function of x. For is, it is supposed that the growth direction of the dendrites is vertical. The maximal extent of the mushy zone occurs at the back of the melt pool and is noted L_{max}. The calculation was repeated for every parameters. As it was explain before, no quantitative correspondence between the simulated dimensions of the melt pool and the experimental one is expected, due to the simplicity of the model (no convection, latent heat, powder addition…). A quantitative validation would require multi-physical models, see for example [32] or [33]. Even the use of a simple model is interesting tough: Figure 8(b) shows a correlation between the maximal extent of the mushy zone predicted by Rosenthal and the crack density. In conditions of high energy (larger melt pool), the thermal gradient is smaller and the mushy zone is deeper. This leads to more solidification cracking, in agreement with RDG model. Note that the markers in color have the same value of L_{max}, because the model does not take into account the effect of the hatching space. Therefore, the model does not account for the decrease of the crack density when the hatching space decreases while P and v_S remain constant (see Figure 4). This effect will be discussed in section 4.5.

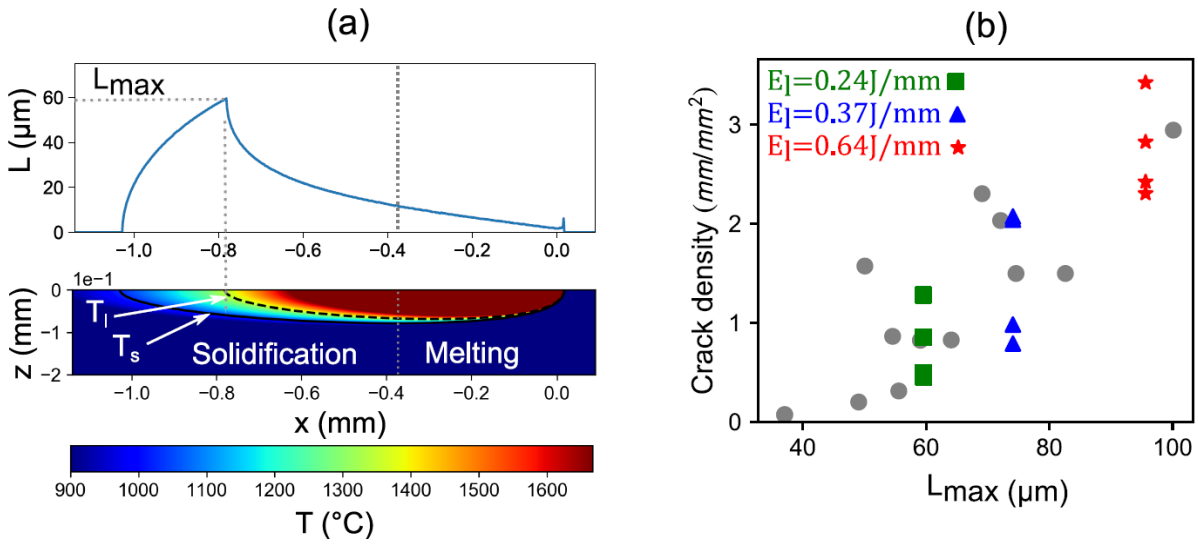

Figure 8 – Correlation between extent of mushy zone and the crack density: (a) Thermal field on a longitudinal section of the melted pool, according to Rosenthal model ($E_l = 0.24 J/mm$). The extent of the mushy L is plotted as a function of x; (b) Correlation between the maximal extent of the mushy zone L_{max} according to Rosenthal and the crack density.

4.3. Mechanical stresses

In welding, solidification cracks are usually longitudinal [34]. It was observed in this study that the cracks always initiate transversally to the melt pool, which is conform to Cloots' observations [8]. As a consequence, the initiation of the cracks is caused by a tensile stress in the direction parallel to scanning direction (longitudinal stress). According to the Rosenthal model, the temperature gradient in the mushy zone is lower for large melt pools. One cannot say that a lesser gradient in this zone means less stress in this region. Indeed, Dye, Hunziker and Reed [35] show with thermomechanical simulations of IN718 welding that the mushy zone is constrained by its surroundings and notably by the heat affected zone. Tensile stress in the mushy zone is the result of differential thermal expansion between the mushy zone and the heat-affected zone. They show that under high linear energy conditions, the contraction of the melt pool during solidification is not compensated by the expansion of the heat-affected zone,

causing a tensile stress in the mushy zone. Although their study considers welding, it is compatible with our observation on the SLM process that there are more cracks when the material is processed with large melt pools.

Although the effect of size of the mushy zone and of the mechanical stresses are useful for the interpretation of the results, it is not sufficient to understand thoroughly the mechanisms at stake in the SLM process. First, the layer-by-layer fabrication produces grains structures which depend strongly on the fabrication parameters [36]. As cracks are known to form more easily on highly disorientated grain boundaries, it is sensible to think that the grain structure has an impact on solidification cracking. Therefore, the role of the grain structure on the cracking density is to be discussed. Moreover, the effect of the overlap ratio on the cracking density observed in this study is not understood at this point.

4.4. Grain structure

It is known in casting and welding processes that solidification cracks appear preferably on high angle grain boundaries (HAGB) [25,37,38]. It has recently been observed on samples additively fabricated with EBM process [15], laser cladding [17] and SLM [8]. Therefore, it is legitimate to think that solidification cracking is highly dependent on the grain structure and that higher angle grain boundaries would result in a higher crack density. To investigate that hypothesis, the grain structure was observed in seven samples (Figure 9). Among the four samples with a linear energy $E_{l1} = 0.24J/mm$ (green square dots), the sample with the minimal and the maximal overlap ratio are respectively noted $E_{l1} - \tau_R^{min}$ and $E_{l1} - \tau_R^{max}$. Similarly, the samples with linear energy of $E_{l2} = 0.37J/mm$ and $E_{l3} = 0.64J/mm$ and with a minimal

and maximal overlap ratio are noted $E_{li} - \tau_R^{min/max}$. Sample E_{l4} corresponds to the additional sample with a minimal cracking density. It was mentioned before that the samples with low energy conditions (on the left of Figure 9) and with a high overlap ratio (on the top) have fewer cracks. Looking at the figure, there is no evident qualitative correlation between the grain structure and the crack density. Indeed, the sample E_{l4} has smaller grains and as a consequence more grains boundaries. It has yet far less cracks than other samples. For further investigation, the grain boundary density function and grain size (major and minor axis of an ellipse fit) were calculated on the full 325 x 900 µm map (Figure 10). The grain boundary density function corresponds to the surface density of grain boundary (in mm/mm²) as a function of the misorientation angle. It is interesting to notice that the sample $E_{l1} - \tau_R^{max}$ exhibits a strong texture along the building direction, with all grains having a <001> crystallographic direction parallel to the building direction. This sample also has fewer grain boundaries with a high misorientation than sample $E_{l1} - \tau_R^{min}$ and is also less cracked. On the contrary, the sample E_{l4} is three times less cracked than the sample $E_{l1} - \tau_R^{max}$, despite having more grain boundaries with high misorientation. Moreover, sample $E_{l3} - \tau_R^{min}$ is about three times more cracked than the samples $E_{l1} - \tau_R^{min}$, although it has less grain boundaries with a high misorientation angle, due to larger grains. Contrary to initial thought, the crack density is not correlated to the density of grain boundaries with a high misorientation. The reason for this is that all samples have a density of highly misorientated grain boundaries (more than 20mm/mm² with an angle over 40°) which is far larger than the crack density (less than 3mm/mm²). Only a small proportion of these grain boundaries features cracks. It is also

interesting to know if the grain size has an influence on the crack density. In aluminum alloys, it is known that small grains lead to a lesser solidification cracking susceptibility [39]. In the case of this study, the sample E_{l4} both features the smallest grain size and the smallest crack density. On the contrary, the grain size does not seem to explain the difference in crack density between samples E_{l1} and E_{l3}. The latter are far more cracked, despite having smaller grains, because it has larger melt pools, see Figure 8. As as conclusion, the grain size is thought to contribute to the crack density, on top of the contribution of the melt pool size.

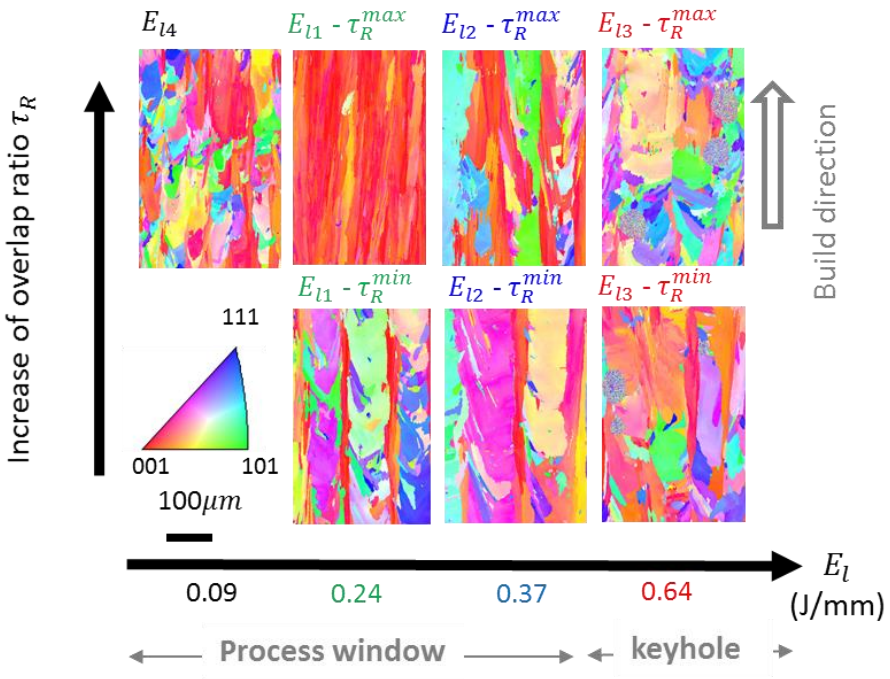

Figure 9 - Grain structure of samples with different fabrication parameters.

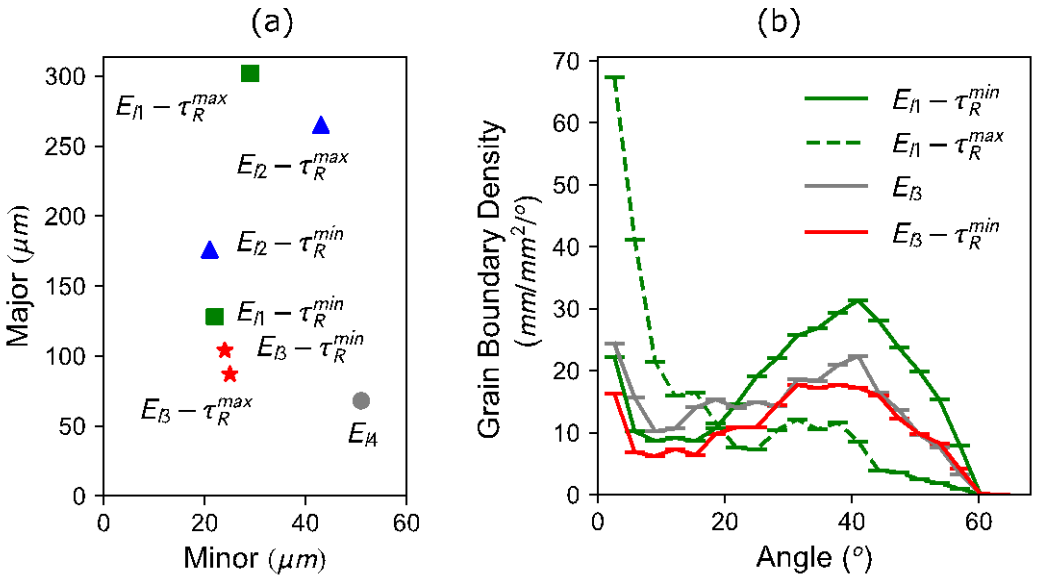

Figure 10 - Grain size of the samples (a) and grain boundary density function (b).

4.5. Overlap ratio

The effect of the overlap between melt pools has not yet been written about. Depending on the fabrication conditions (low or high linear energy), Carter et al. [9] measure either an increase or a decrease of microcracking with the hatching space. In this study, a decrease of the microcracking with hatching space was observed in any cases. During the fabrication of a layer, the material which is solidified in a melt pool is then partially remelted during the fusion of the adjacent melt pool. The more overlap, the more remelting. With an observation of the upper layer, it was noticed that cracks do not propagate again in the adjacent melt pool during its solidification (Figure 11.a). As a consequence, remelting repairs partially the cracks. It can be understood with Figure 11.b that a higher overlap will induce narrower cracks. Narrow cracks are likely to have a lower probability of propagation in higher fabrication layers, as it was observed in Figure 3. This provides a possible explanation for the effect of the overlap ratio on the cracking density.

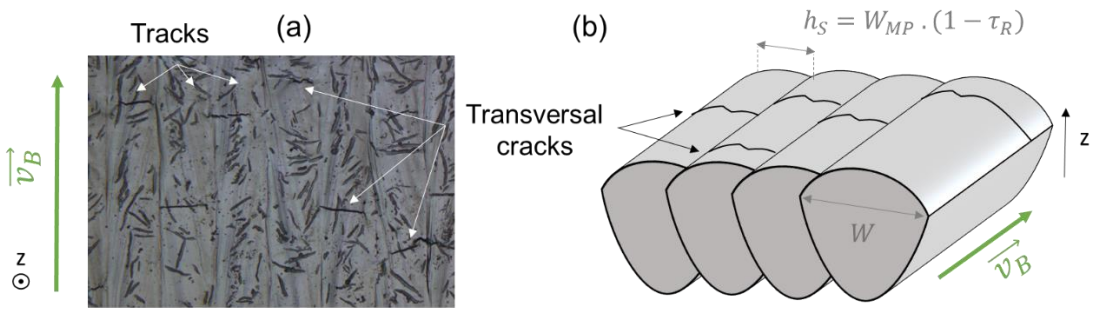

Figure 11 – Effect of overlap on crack repair : (a) cracks visible on the upper layer of a sample (top view) ; (b) partial repair of cracks by remelting.

Conclusions

The goal of this study was to link the fabrication parameters, the geometry of the melt pools and the occurrence of solidification cracking. It was shown that larger melt pools lead to more microcracking. With the same melt pool width, more overlap leads to less cracking, which was attributed to a partial repair of cracks by remelting. These findings have made possible the fabrication of a dense and crack free material, by controlling the melt pool size combined with a control of the overlap ratio. The difference in cracking density is not a consequence of a difference in high-angle grain boundaries density, but can be partially explained by the grain size, with a beneficial effect of small grains. Beside this contribution and the contribution of the repair by remelting, the difference of cracking is thought to be mostly a consequence of the size of the mushy zone and the intensity of the mechanical stresses. As a conclusion, using narrow melt pools with a large overlap and parameters that produce fine grains are promising routes to suppress hot cracking in additively manufactured high performance Ni-based superalloys.

Acknowledgments

Safran Tech (Châteaufort, France) funded this study.

References

[1] R.C. Reed, The Superalloys: Fundamentals and Applications, Cambridge University Press, Cambridge, 2006. https://doi.org/10.1017/CBO9780511541285.

[2] M.J. Donachie, S.J. Donachie, Superalloys: A Technical Guide, 2nd Edition, ASM International, 2002.

[3] A.T. Egbewande, H.R. Zhang, R.K. Sidhu, O.A. Ojo, Improvement in Laser Weldability of Inconel 738 Superalloy through Microstructural Modification, Metall. Mater. Trans. A. 40 (2009) 2694. https://doi.org/10.1007/s11661-009-9962-6.

[4] O.A. Ojo, N.L. Richards, M.C. Chaturvedi, Liquation of various phases in HAZ during welding of cast Inconel 738LC, Mater. Sci. Technol. 20 (2004) 1027–1034. https://doi.org/10.1179/026708304225019948.

[5] J.E. Franklin, W.F. Savage, Stress relaxation and strain-age cracking in Rene 41 weldments, Weld J N. 53 (1974) 380–387.

[6] M. Rowe, Ranking the resistance of wrought superalloys to strain-age cracking, Weld. J. 85 (2006) 27–33.

[7] R. Engeli, T. Etter, S. Hövel, K. Wegener, Processability of different IN738LC powder batches by selective laser melting, J. Mater. Process. Technol. 229 (2016) 484–491. https://doi.org/10.1016/j.jmatprotec.2015.09.046.

[8] M. Cloots, P.J. Uggowitzer, K. Wegener, Investigations on the microstructure and crack formation of IN738LC samples processed by selective laser melting using Gaussian and doughnut profiles, Mater. Des. 89 (2016) 770–784.

[9] L.N. Carter, M.M. Attallah, R.C. Reed, Laser powder bed fabrication of nickel-base superalloys: influence of parameters; characterisation, quantification and mitigation of cracking, in: Proc 12th Int Symp Superalloys Champion PA 9–13 Sept. 2012, 2012: pp. 577–586.

[10] D. Tomus, P.A. Rometsch, M. Heilmaier, X. Wu, Effect of minor alloying elements on crack-formation characteristics of Hastelloy-X manufactured by selective laser melting, Addit. Manuf. 16 (2017) 65–72. https://doi.org/10.1016/j.addma.2017.05.006.

[11] N.J. Harrison, I. Todd, K. Mumtaz, Reduction of micro-cracking in nickel superalloys processed by Selective Laser Melting: A fundamental alloy design approach, Acta Mater. 94 (2015) 59–68. https://doi.org/10.1016/j.actamat.2015.04.035.

[12] K. Kunze, T. Etter, J. Grässlin, V. Shklover, Texture, anisotropy in microstructure and mechanical properties of IN738LC alloy processed by selective laser melting (SLM), Mater. Sci. Eng. A. 620 (2015) 213–222. https://doi.org/10.1016/j.msea.2014.10.003.

[13] T. Etter, R. Engeli, A. Kuenzler, Method for post-built heat treatment of additively manufactured components made of gamma-prime strengthened superalloys, US9670572B2, 2015.

[14] J.H. Boswell, D. Clark, W. Li, M.M. Attallah, Cracking during thermal post-processing of laser powder bed fabricated CM247LC Ni-superalloy, Mater. Des. 174 (2019) 107793. https://doi.org/10.1016/j.matdes.2019.107793.

[15] E. Chauvet, P. Kontis, E.A. Jägle, B. Gault, D. Raabe, C. Tassin, J.-J. Blandin, R. Dendievel, B. Vayre, S. Abed, G. Martin, Hot cracking mechanism affecting a non-weldable Ni-based superalloy produced by selective electron Beam Melting, Acta Mater. 142 (2018) 82–94. https://doi.org/10.1016/j.actamat.2017.09.047.

[16] M. Gäumann, C. Bezençon, P. Canalis, W. Kurz, Single-crystal laser deposition of superalloys: processing–microstructure maps, Acta Mater. 49 (2001) 1051–1062. https://doi.org/10.1016/S1359-6454(00)00367-0.

[17] J. Xu, X. Lin, P. Guo, H. Dong, X. Wen, Q. Li, L. Xue, W. Huang, The initiation and propagation mechanism of the overlapping zone cracking during laser solid forming of IN-738LC superalloy, J. Alloys Compd. 749 (2018) 859–870. https://doi.org/10.1016/j.jallcom.2018.03.366.

[18] I. Yadroitsev, P. Krakhmalev, I. Yadroitsava, S. Johansson, I. Smurov, Energy input effect on morphology and microstructure of selective laser melting single track from metallic powder, J. Mater. Process. Technol. 213 (2013) 606–613. https://doi.org/10.1016/j.jmatprotec.2012.11.014.

[19] H. Gu, H. Gong, D. Pal, K. Rafi, T. Starr, B. Stucker, Influences of energy density on porosity and microstructure of selective laser melted 17-4PH stainless steel, in: 2013 Solid Free. Fabr. Symp., 2013.

[20] K. Darvish, Z.W. Chen, T. Pasang, Reducing lack of fusion during selective laser melting of CoCrMo alloy: Effect of laser power on geometrical features of tracks, Mater. Des. 112 (2016) 357–366. https://doi.org/10.1016/j.matdes.2016.09.086.

[21] W.E. King, H.D. Barth, V.M. Castillo, G.F. Gallegos, J.W. Gibbs, D.E. Hahn, C. Kamath, A.M. Rubenchik, Observation of keyhole-mode laser melting in laser powder-bed fusion additive manufacturing, J. Mater. Process. Technol. 214 (2014) 2915–2925. https://doi.org/10.1016/j.jmatprotec.2014.06.005.

[22] I. Yadroitsev, I. Smurov, Surface Morphology in Selective Laser Melting of Metal Powders, Phys. Procedia. 12 (2011) 264–270. https://doi.org/10.1016/j.phpro.2011.03.034.

[23] I. Yadroitsev, A. Gusarov, I. Yadroitsava, I. Smurov, Single track formation in selective laser melting of metal powders, J. Mater. Process. Technol. 210 (2010) 1624–1631. https://doi.org/10.1016/j.jmatprotec.2010.05.010.

[24] O.M.D.M. Messé, R. Muñoz-Moreno, T. Illston, S. Baker, H.J. Stone, Metastable carbides and their impact on recrystallisation in IN738LC processed by selective laser melting, Addit. Manuf. 22 (2018) 394–404. https://doi.org/10.1016/j.addma.2018.05.030.

[25] J.A. Dantzig, M. Rappaz, Deformation during solidification and hot tearing, in: Solidification, EPFL press, 2009.

[26] T. Clyne, G. Davies, Influence of composition on solidification cracking susceptibility in binary alloy systems, Br. Foundrym. 74 (1981) 65–73.

[27] M. Rappaz, J.-M. Drezet, M. Gremaud, A new hot-tearing criterion, Metall. Mater. Trans. A. 30 (1999) 449–455. https://doi.org/10.1007/s11661-999-0334-z.

[28] D. Rosenthal, The theory of moving sources of heat and its application of metal treatments, Trans. ASME. 68 (1946) 849–866.
[29] P.N. Quested, R.F. Brooks, L. Chapman, R. Morrell, Y. Youssef, K.C. Mills, Measurement and estimation of thermophysical properties of nickel based superalloys, Mater. Sci. Technol. 25 (2009) 154–162. https://doi.org/10.1179/174328408X361454.
[30] J.V. Wood, P.F. Mills, A.R. Waugh, J.V. Bee, Rapidly solidified nickel-base superalloys, J. Mater. Sci. 15 (1980) 2709–2719. https://doi.org/10.1007/BF00550537.
[31] L. Liu, F. Sommer, H.Z. Fu, Effect of solidification conditions on MC carbides in a nickel-base superalloy IN 738 LC, Scr. Metall. Mater. 30 (1994) 587–591. https://doi.org/10.1016/0956-716X(94)90434-0.
[32] L. Moniz, Q. Chen, G. Guillemot, M. Bellet, C.-A. Gandin, C. Colin, J.-D. Bartout, M.-H. Berger, Additive manufacturing of an oxide ceramic by laser beam melting—Comparison between finite element simulation and experimental results, J. Mater. Process. Technol. 270 (2019) 106–117. https://doi.org/10.1016/j.jmatprotec.2019.02.004.
[33] T.T. Roehling, S.S.Q. Wu, S.A. Khairallah, J.D. Roehling, S.S. Soezeri, M.F. Crumb, M.J. Matthews, Modulating laser intensity profile ellipticity for microstructural control during metal additive manufacturing, Acta Mater. 128 (2017) 197–206. https://doi.org/10.1016/j.actamat.2017.02.025.
[34] T. Böllinghaus, H. Herold, C.E. Cross, J.C. Lippold, eds., Hot Cracking Phenomena in Welds II, Springer Berlin Heidelberg, Berlin, Heidelberg, 2008. https://doi.org/10.1007/978-3-540-78628-3.
[35] D. Dye, O. Hunziker, R.C. Reed, Numerical analysis of the weldability of superalloys, Acta Mater. 49 (2001) 683–697. https://doi.org/10.1016/S1359-6454(00)00361-X.
[36] L. Thijs, K. Kempen, J.-P. Kruth, J. Van Humbeeck, Fine-structured aluminium products with controllable texture by selective laser melting of pre-alloyed AlSi10Mg powder, Acta Mater. 61 (2013) 1809–1819. https://doi.org/10.1016/j.actamat.2012.11.052.
[37] N. Wang, S. Mokadem, M. Rappaz, W. Kurz, Solidification cracking of superalloy single- and bi-crystals, Acta Mater. 52 (2004) 3173–3182. https://doi.org/10.1016/j.actamat.2004.03.047.
[38] M. Rappaz, A. Jacot, W.J. Boettinger, Last-stage solidification of alloys: Theoretical model of dendrite-arm and grain coalescence, Metall. Mater. Trans. A. 34 (2003) 467–479. https://doi.org/10.1007/s11661-003-0083-3.
[39] M.G. Mousavi, C.E. Cross, Ø. Grong, Effect of scandium and titanium–boron on grain refinement and hot cracking of aluminium alloy 7108, Sci. Technol. Weld. Join. 4 (1999) 381–388. https://doi.org/10.1179/136217199101538030.

Annex: initial manuscript

Processing of a non-weldable Nickel-base superalloy by Laser Beam Melting: role of the shape and size of the melt pools on solidification cracking

D. Grange[a,b*], J-D. Bartout[a], B. Macquaire[b], C. Colin[a]

[a]MINES ParisTech, PSL Research University, MAT – Centre des matériaux, CNRS UMR 7633, BP 87 91003 Evry, France

[b]Safran Additive Manufacturing, a technology platform of Safran Tech, Rue des Jeunes Bois, Châteaufort, 78114 Magny-Les-Hameaux, France

Abstract

The use of laser-based additive manufacturing for the fabrication of parts exposed to very high temperature in the aerospace and energy sectors is still very limited. Indeed, non-weldable superalloys tend to crack during their processing by Laser Beam Melting (LBM). Inconel 738 LC processed by LBM is subjected to solidification cracking. In this study, attention is focused on the influence of size and shape of the melt pools involved in the fabrication on the occurrence of cracking. This approach is motivated by the fact that the size and shape of the melt pools greatly affect the solidification conditions. Samples were fabricated with various fabrication parameters, leading to different melt pool sizes and shapes and different cracking intensity. It is

* Corresponding author at *MINES ParisTech, Centre des matériaux, 91003 Evry, France.* Tel.: (+33) 6 37 30 74 54; Email address: david.grange@mines-paristech.fr

shown that the cracking is minimal when the fabrication uses narrow melt pools and a strong overlap between adjacent melt pools. These observations were discussed in the light of solidification theory. As the cracks are known to appear primarily at high-angle grain boundaries, the effect of grain structure is investigated. These observations allowed the fabrication of a dense and crack-free material. Finally, the effect of composition is discussed, based on a comparison with another superalloy containing the same amount of γ' precipitates.

Keywords: Selective laser melting (SLM), Nickel-base superalloy, IN738 LC, Solidification cracking, Melt pool

---

5. Introduction

Shaping hard metals with a laser beam is a complicated exercise. For years, precipitation hardening of nickel-base superalloys has been widely used in aerospace and energy sectors for the fabrication of parts with an exceptional high-temperature strength. Although these materials were initially designed for casting, there is today a strong industrial interest in being able to shape them with the laser beam melting (LBM) process. A reinforcement of the γ matrix by a volume fraction of γ'-Ni_3(Al, Ti) precipitates between 40% and 80% is necessary for high-temperature properties [1,2], but this reinforcement unfortunately also increases the susceptibility of the materials to cracking during either their melting by a laser source or during further heat-treatments. Welding literature describes a typology of cracks that includes solidification cracking, ductility dip, liquation or strain age cracking [3–6]. There is today active research on the best way to fabricate defect-free parts using laser-based additive manufacturing processes.

In previous studies, microscopic solidification cracks were observed on samples produced by LBM with different alloys: IN738 LC [7,8], CM247 LC [9] and Hastelloy X [10,11]. These defects are problematical: only the ones located in the bulk of the material can be healed with a hot isostatic pressing (HIP) treatment, whereas surface cracks will remain open. Kunz, Etter, Grässlin and Shklover [12] reported that they were able to produce samples in IN738 LC for mechanical tests without cracks, with a HIP treatment. It was possible because the specimens were machined and thus the surface cracks were removed. Nevertheless, the scaled-up production of net shape parts with that solution is not possible.

A first possible solution to prevent cracking is to control or modify the alloy composition. Several authors focused on the role of minor elements in various alloys. Engeli, Etter, Hövel and Wegener [7] processed by LBM with the same fabrication parameters eight batches with different compositions in the specification range of Inconel 738 LC. They calculated the correlation between the crack density and the composition in thirty-one minor elements. They concluded that there is a strong detrimental effect of elements Si and Pb. Cloots, Uggowitzer and Wegener [8] measured the segregation profile of minor elements at grain boundaries after solidification and suggest an effect of Zr and B on cracking susceptibility. Tomus, Rometsch, Heilmaier and Wu [10] proposed that Si, Mn and C have a strong influence on solidification cracking of Hastelloy X. Chauvet et al. [13] observed the presence of phases rich in B at grain boundaries with a superalloy (Ti + Al=8.6 wt%) processed by Electron Beam Melting (EBM) and concluded in an important role of these phases. At this point, there is a general agreement on an effect of minor elements, but conclusions sometimes differ when it comes to ranking the effect of the different elements. Moreover, several authors underline that some minor elements (B and C) are useful for high temperature mechanical properties.

A second possible solution is an optimization of the fabrication parameters. Some studies investigate the effect of the fabrication parameters on solidification cracking. Carter, Attallah and Reed [9] noted a decrease in the cracking density of samples in CM247 LC when the scanning velocity of the laser beam was increased. They also observed an ambiguous role of the hatching space, which is the distance between two scanning tracks. Depending on the other fabrication parameters, an increase of the hatching space resulted either in more cracks or less

cracks. In the same way, Cloots et al. [8] observed with a fixed laser power ($P = 200W$) and a fixed hatching space that an increase of the scanning speed resulted in less cracks but also more porosity. He concluded that there is a necessary compromise between suppressing microcracking and having a dense material. To optimize the fabrication with the LBM process, it is worth remembering that the interaction of the laser beam with the powder bed creates a pool of liquid metal (melt pool), whose geometry depends very strongly on the fabrication parameters. This geometry is very important because it determines the solidification conditions [14] (solidification gradient G and solidification velocity v_S) at the origin of microstructures and defects as pores and solidification cracks. So far, no study has focused on the link between the shape or size of the melt pool and the microcracking phenomena. The objective of the present work is to elucidate the link between the process parameters, the geometry or size of melt pools and the occurrence of the defects. The main finding is that it is possible to simultaneously avoid cracks and obtain a dense material, by a control of the melt pool size combined with a control of the overlap between melt pools. The effect of the grain structure and of the mechanical stresses were also investigated. Although the work mainly focuses on Inconel 738 LC, the effect of the composition is discussed, based on a comparison with another material.

6. Experiments

6.1. Fabrication conditions

For the fabrication of the specimens, a gas-atomized IN738 LC powder was used with a composition given in Table 1. The particle size distribution is gaussian, with diameter

percentiles $D_{10} = 17\mu m$, $D_{50} = 28\mu m$, $D_{90} = 45\mu m$. The specimens are 10mm cubes, fabricated using a Concept Laser M2 machine. They were built on a plate in IN625 on a 2mm height of lattice supports in order to facilitate cutting after fabrication. All the samples have in common the following fabrication parameters: a layer thickness ΔZ = 40µm, a laser beam $1/e^2$ diameter $\phi_L =$ 100µm and a bidirectional scanning pattern with a rotation of 90° of scanning direction between each layer (Figure 1.a). This scanning pattern was chosen to facilitate observation of the melt pools. The variable parameters are the laser power P (85 – 370W), the scanning speed v_L (380 – 1600mm/s) and the hatching space h_s (75 - 195μm). Figure 1.b represents graphically the value of the fabrication parameters in a coordinate reference $(v_L/v_L^{max}, P/P^{max})$, and in a reference (E_l, h_S), where E_l = P / v_L is the linear incident energy on the powder bed. The dots noted with squares, triangles or stars correspond to pairs (P, v_L) that have been used with several values of the hatching space. On the graph on the right, an increase in hatching space as a function of the linear energy is visible. This choice, based on previous experience, will be discussed further in the article.

	Cr	Ni	Co	Mo	W	Nb	Ta	Ti	Al	B	C	Fe	Si	Cu	Zr
IN738 LC	16.1	Bal	8.82	1.78	2.61	0.85	1.75	3.37	3.46	0.01	0.10	0.05	0.048	0.001	0.063
René 77	14.5	Bal	14.5	4.27				3.55	4.38	0.02	0.067	0.043	0.023	9.10^{-4}	8.10^{-5}

Table 3 – Weight composition in percent of Inconel 738 LC and René 77

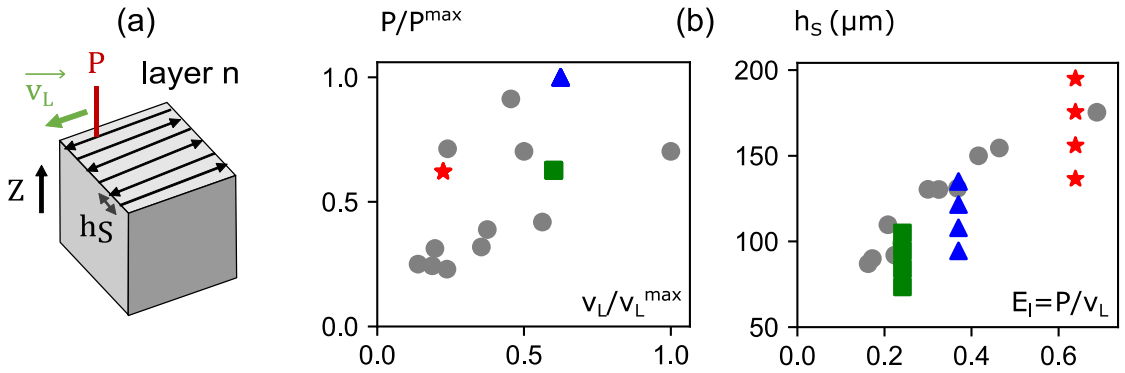

Figure 12 – Fabrication parameters : (a) schematic representation of primary process parameters ; (b) values of parameters used in this work.

6.2. Crack observation

The nature of the cracks was identified on the sample with $E_l = 0.24J/mm$ and $h_S = 105\mu m$. The fabrication and observation conditions are detailed afterwards. After a midplane cut, Electron Back Scattered Diffraction (EBSD) was performed in a FEI Nova NanoSEM 450 with an EDAX Hikari EBSD camera. The acceleration tension was 20kV and the probe current was 10nA. An EBSD map of size 325 x 950 μm was taken at the center of the top of the sample. The data was analyzed using the OIM Analysis™ v7 software. Microscopic cracks are visible on Figure 2.a: they measure typically $100\mu m$ and are mainly vertical and located at grain boundaries. The crack surface was examined after bending the sample up to failure, see Figure 2.b. Was used for observation, a Zeiss Gemini Sigma 300 Scanning Electron Microscope (SEM) with an Everhart-Thornley secondary electron (SE) detector and an acceleration tension of 5kV. Dendritic microstructures are visible on the fracture surface. This is a sign of the presence of residual interdendritic liquid when the crack was formed. As other authors have concluded, this material processed by LBM is subjected to solidification cracking [7,8,15].

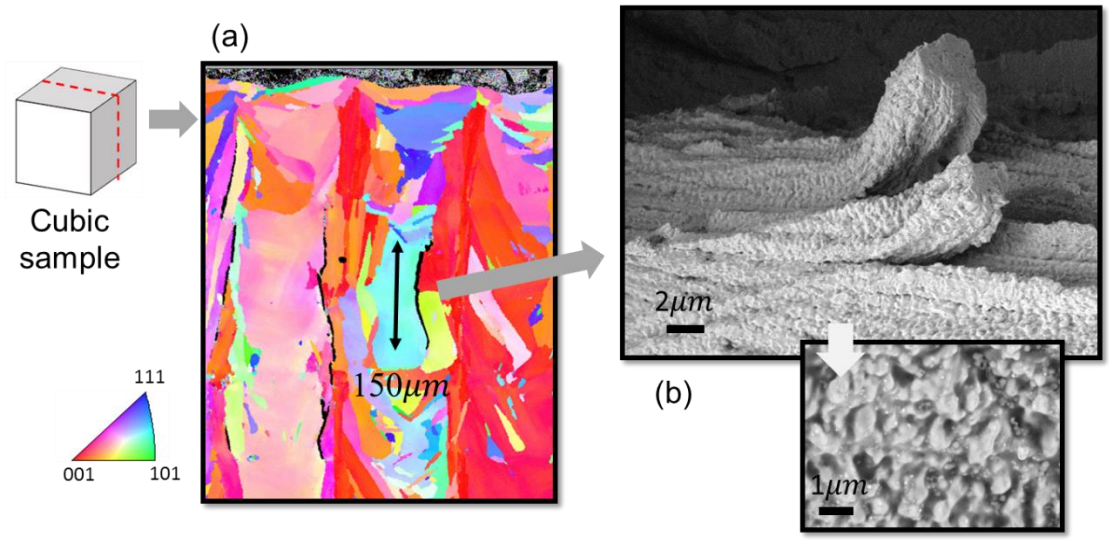

Figure 13 - Solidification cracking of an Inconel 738 sample processed by LBM: (a) microscopic vertical cracks located at grain boundaries, (b) dendritic microstructure visible on the crack surface, sign of residual liquid during the cracking.

6.3. Melt pool shape and size

The melt pools are revealed with a Glycerigia etching followed by an observation with an optical microscope, see Figure 3.a. The fabrication pattern is well visible on the image. Because of the 90° rotation of the scanning speed vector $\overrightarrow{v_L}$ between two fabrication layers, the cut shows transversal sections of the melt pools in a layer and longitudinal sections in the next layer. A crack is visible: it initiates in a layer, transversally to a melt pool, and then propagates in several higher layers. As explained before, the objective of this study is to link the occurrence of these defects within the melt pool geometry on a large set of fabrication parameters. For that purpose, some characteristic dimensions of the melt pools (Figure 3.b) are measured in the top layer of the sample: the melt pool width W_{MP} and the height of the remelting zone H_{RZ}. Measures are taken on ten adjacent melt pools in the center of the sample. Let us note that a melt pool is never fully visible as it has been partially remelted by the following one. As a consequence, the half width on the left-side of the melt pool, which is always visible, was

measured. Figure 3.c shows the evolution of W_{MP} and H_{RZ} with respect to the linear energy $E_l = P/v_L$ (J/mm) and to the hatching space h_S. In LBM process as in welding, it is common knowledge that melt pool size increases with respect to linear energy [16], up to the *keyhole* regime (vaporization), which is inappropriate for LBM. An effect of the hatching space on the melt pool dimensions was also observed, especially for high energy fabrication parameters ($E_l > 0.3J/mm$). The overlap ratio τ_R depends both on W_{MP} and h_S:

$$\tau_R = 1 - \frac{h_S}{W_{MP}} \qquad \text{Equation 2}$$

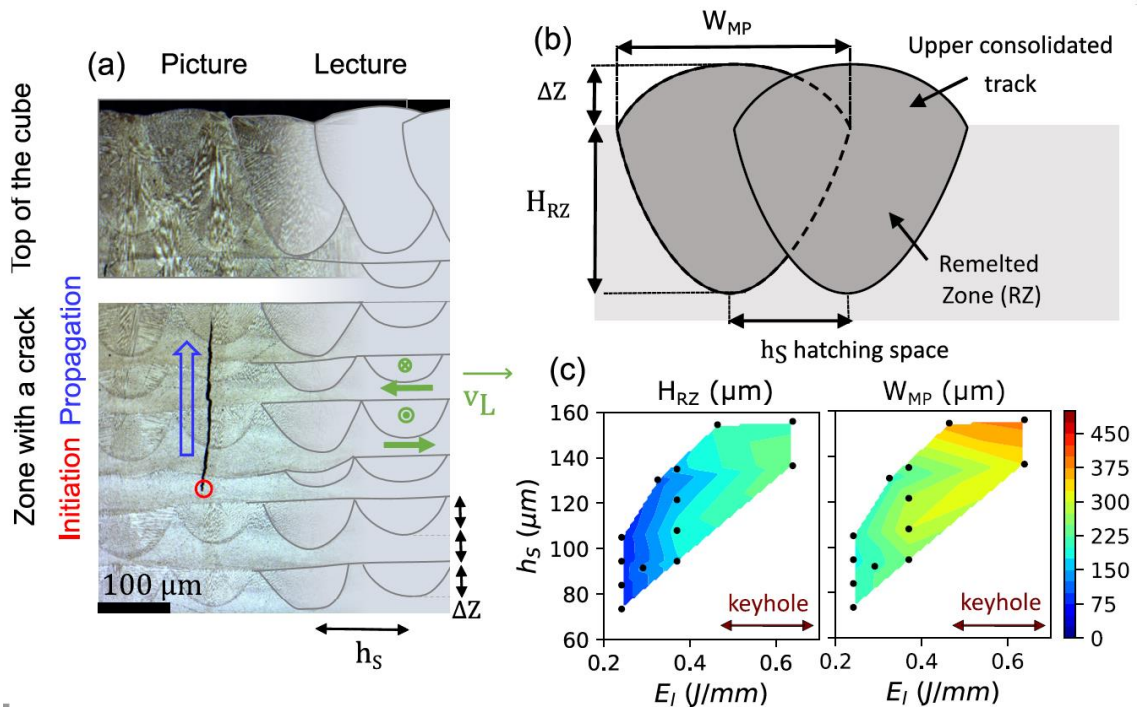

Figure 14 – (a) Initiation of a microcrack transversally to the melt pool and propagation in higher layers ; (b) Some geometrical features of melt pools ; (c) Melt pool width W_{MP} and remelted zone height H_{RZ} as a function of linear energy $E_l = P/v_L$ and hatching space h_S.

6.4. Crack quantitative analysis and microstructure observation

For a quantitative analysis of cracks with the best statistical reliability, a cartography of the whole 10mm x 10mm midplane section of each cube was performed with a Keyens optical microscope. A polishing down to $0.04\mu m$ colloidal silica finish enabled the detection of thin ($1\mu m$ wide) cracks and a good contrast necessary for image analysis. A processing with the software ImageJ allowed to distinguish the different types of defects (cracks and pores), with meticulous visual verification after the processing of every image. As a result, a crack density, that is to say a cumulative length of cracks per unit area (in mm/mm²), was calculated for every sample. In the same way, a fraction area of pores was evaluated. Microstructure observation was performed with a Zeiss Gemini Sigma 300 SEM and with an In-Lens secondary electron detector, after a Glycerigia etching.

7. Results

7.1. Cracking

The samples exhibit a very wide range of crack density: the most heavily cracked sample has a density of 3.5mm/mm² whereas the best sample is 18 times less cracked (0.2mm/mm²) and only features a few cracks on its sides. It confirms the very strong influence of fabrication parameters on cracking. Correlations between the crack density and criteria based on the process parameters ($P, v_L, h_S, E_l,\ E_V = P/(v_L.h_S.\Delta Z)$[2]) or based on the dimensions of the melt pools ($W_{MP}, H_{RZ}, H_{RZ}/\Delta Z,\ H_{RZ}/W_{MP}$) were investigated. The best correlation found is between the

[2] This criterion corresponds to a volumetric energy density (J/mm^3), often used in the LBM process [17,18].

crack density and the hatching space h_S, which is presented on Figure 4. The lesser the hatching space, the fewer cracks. To interpret this correlation, it is recalled that:

$$h_S = W_{MP}^{(1)} \times (1 - \tau_R)^{(2)}, \quad \text{Equation 2}$$

where τ_R is the overlap ratio defined in Equation 1. This let us note two contributions for this trend:

3) *Effect of the melt pool width* W_{MP}: the density of cracks decreases when the melt pools are narrower (W_{MP} is smaller). Given the result of Figure 3.c, this is equivalent to saying that the density of cracks decreases when the linear energy E_l decreases. On Figure 4, the red dots (stars) correspond to a superior linear energy (0.64J/mm) than the green dots (squares) and their crack density is about three times higher.
4) *Effect of the overlap*: at equal melt pool size, the crack density drops when the overlap between the melt pools rises. For example, the green dots (squares) all have a linear energy of 0.24J /mm and width $W_{MP} = 200 \pm 10\mu m$. Among these points, a higher overlap ratio τ_R (i.e. a smaller hatching space h_S) leads to less cracking. The same trend is valid for blue dots (triangles) and red dots (stars).

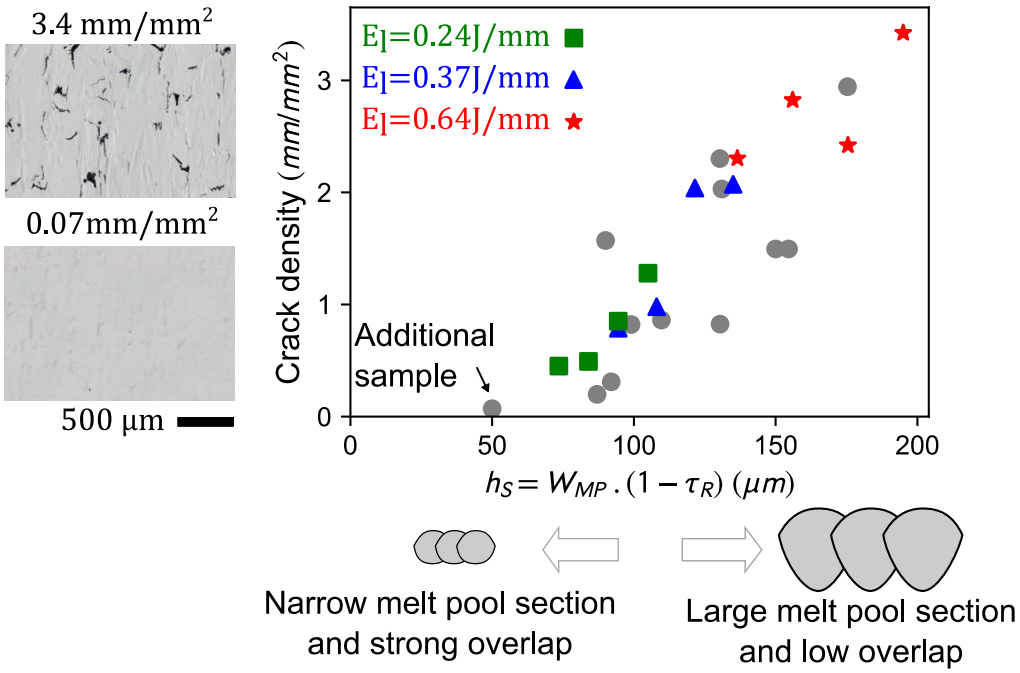

Figure 15 - Effect of fabrication parameters on the crack density.

Following this finding, an additional sample was fabricated with a very low linear energy ($E_l = 0.09J/mm$) and a very low hatching space. As expected, it features the lowest crack density: 0.07mm/mm², with only a few cracks located close to the free faces of the cube.

7.2. Porosity

Porosity in samples has different origins. First, round pores were observed for high linear energies ($E_l > 0.45J/mm$). They are typical of keyhole porosity, caused by the vaporization of the metal [19]. Second, irregularities of the upper surface of the cubes known as humping phenomena [20] were observed at low and high scanning velocities ($v_L < 400mm/s$ and $v_L > 1600mm/s$). These irregularities lead to an inhomogeneous powder bed thickness, so that the powder bed in some locations is too thick to be fully melted by the laser beam. This leads to a porosity called lack of fusion. Third, lack of fusion porosity also occurs when the overlap ratio between adjacent melt pools is too low, so that some amount of powder remain

unmelted between them [18]. An example of pores resulting from keyhole regime and lack of fusion are visible on Figure 5.a. Figure 5.b represents the surface fraction of pores as a function of the overlap ratio, for the samples that were not affected by keyhole porosity or by upper surface irregularities. One can see that a relative density over 99.9% is achievable by using an overlap ratio over 0.4. Given Equation 1, the values of the hatching space h_S suitable for the fabrication increase with E_l, as shown in Figure 1. Unlike the conclusion of Cloots et al. [8], it was possible to produce a sample with both a low cracking density and a low porosity. This is possible by decreasing not only P/v_L, but also the hatching space h_S in parallel (see Figure 1.b), to obtain a sufficient overlap ($\tau_R = 40\%$) and thus a low porosity. For example, the additional sample which features the minimal microcracking density also has a relative density over 99.9%.

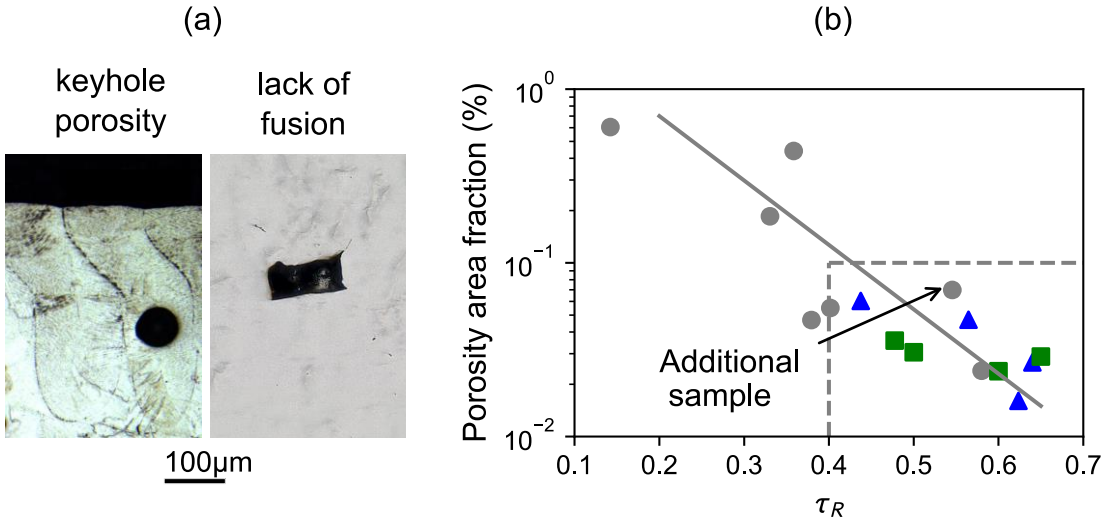

Figure 16 – (a) Keyhole porosity and lack of fusion porosity on samples; (b) Relation between the overlap ratio and the surface fraction of pores. The samples affected by keyhole or humping phenomenon are not represented on the graph.

7.3.

7.4. Microstructure

The as-built specimens exhibit a very thin microstructure (Figure 6), with a primary dendrite arm spacing (PDAS) $\lambda_1 \sim 600nm$ and TiC carbides in interdendritic regions with a size inferior to 200nm, as observed in Ref. [21]. Despite a composition rich in γ'-forming elements (Al+Ti+Ta+Nb >13% at), potential γ' precipitates are too small to be visible with a 50 000 magnification and the In-Lens detector.

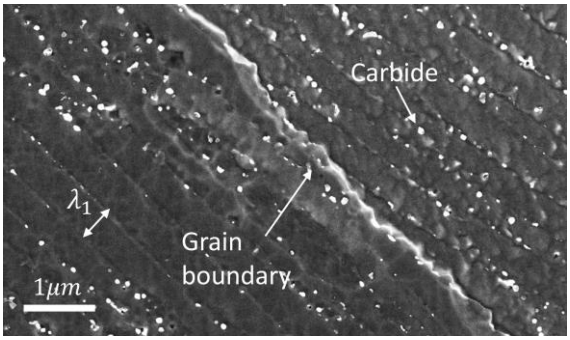

Figure 17 - Microstructure on one of the samples (0.24J/mm) observed with a SEM In Lens SE Detector.

8. Discussion

8.1. Solidification cracking mechanism

In casting and welding processes, solidification is known to occur under two necessary conditions: mechanical stresses in the mushy zone and insufficient liquid feeding in a brittle temperature range (BTR), at the end of solidification (see Figure 7), between two characteristic values of solid fraction f_s. In the corresponding temperature range, the solid dendritic network is coherent [22], allowing mechanical stresses to be transmitted . A tensile stress between grains can still separate them, because a liquid film between them remains. If the available liquid pressure is not high enough, the separation causes a rupture of the liquid film and then a crack to appear. Despite the general agreement that the brittle temperature range is close to the end of

solidification, the critical values of f_s differ between authors. For example, Clyne and David suggested that the alloy is brittle when f_s is comprised between 0.9 and 0.99 [23].

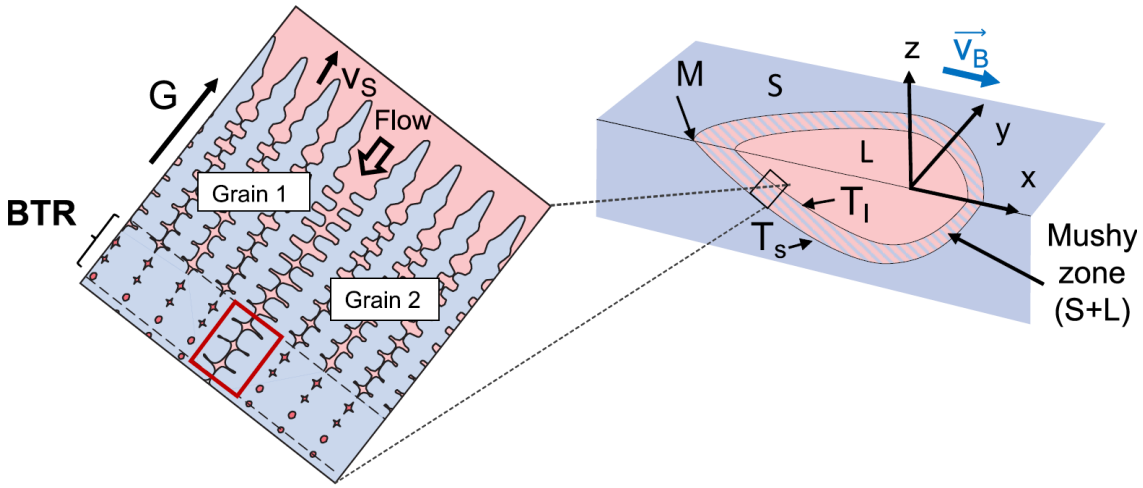

Figure 18 - Solidification cracking mechanism, adapted from Dantzig and Rappaz [22] : T_l is the liquidus temperature, T_s the solidus temperature and v_s the liquidus isotherm velocity.

The thermal gradient in the mushy zone can be estimated with Rosenthal model [24], which gives the thermal field $T(x,y,z)$ around the punctual moving laser source:

$$T - T_{sub} = \frac{A.P}{2\pi kr}\exp\left(-\frac{v_L(r+x)}{2\alpha}\right) \qquad \text{Equation 3}$$

where T_{sub} is the substrate temperature far from the melt pool, A the absorption coefficient, $r = \sqrt{x^2+y^2+z^2}$, k the material thermal conductivity and α the material thermal diffusivity. One can calculate the gradient at the solidus isotherm T_s on the centerline at the end of the melt pool (point M):

$$\frac{\partial T}{\partial x}(T = T_s) = \frac{2\pi k}{A.P}(T_s - T_{sub})^2 \qquad \text{Equation 4}$$

With a high power, the thermal gradient is smaller, causing the mushy zone (i.e. with a temperature between liquidus and solidus) to be wider. Moreover, energy conservation says that the melt pool cross section is proportional to $A.P/V$. In conditions of high energy, large melt

pools result in a wider mushy zone, more sensitive to solidification cracking, in agreement with the results.

Although this tendency can be interpreted thanks to an analogy with welding literature, it is not sufficient to understand thoroughly the mechanisms at stake in the LBM process. First, the layer-by-layer fabrication produces grains structures which depend strongly on the fabrication parameters [25]. As cracks are known to form more easily on highly disorientated grain boundaries, it is sensible to think that the grain structure has an impact on solidification cracking. Therefore, the role of the grain structure on the cracking density is to be discussed. Moreover, the effect of the overlap ratio on the cracking density observed in this study is not understood at this point.

8.2. Grain structure

It is known in casting and welding processes that solidification cracks appear preferably on high angle grain boundaries (HAGB) [22,26,27]. It has recently been observed on samples additively fabricated with EBM process [13], laser cladding [15] and LBM [8]. Therefore, it is legitimate to think that solidification cracking is highly dependent on the grain structure and that higher angle grain boundaries would result in a higher crack density. To investigate that hypothesis, the grain structure was observed in seven samples (Figure 9). Among the four samples with a linear energy $E_{l1} = 0.24J/mm$ (green square dots), the sample with the minimal and the maximal overlap ratio are respectively noted $E_{l1} - \tau_R^{min}$ and $E_{l1} - \tau_R^{max}$. Similarly, the samples with linear energy of $E_{l2} = 0.37J/mm$ and $E_{l3} = 0.64J/mm$ and with a minimal and maximal overlap ratio are noted $E_{li} - \tau_R^{min/max}$. Sample E_{l4} corresponds to the

additional sample with a minimal cracking density. It was mentioned before that the samples with low energy conditions (on the left of Figure 9) and with a high overlap ratio (on the top) have fewer cracks. Looking at the figure, there is no evident qualitative correlation between the grain structure and the crack density. Indeed, the sample E_{l4} has smaller grains and as a consequence more grains boundaries. It has yet far less cracks than other samples. For further investigation, the grain boundary density function and grain size (major and minor axis of an ellipse fit) were calculated on the full 325 x 900 µm map (Figure 10). The grain boundary density function corresponds to the surface density of grain boundary (in mm/mm²) as a function of the misorientation angle. It is interesting to notice that the sample $E_{l1} - \tau_R^{max}$ exhibits an orientated grain structure, with all grains having a 001 crystallographic orientation parallel to the building direction. As a consequence, this sample has fewer grain boundaries with a high misorientation than sample $E_{l1} - \tau_R^{min}$ and is also less cracked. On the contrary, the sample E_{l4} is three times less cracked than the sample $E_{l1} - \tau_R^{max}$, despite having more grain boundaries with high misorientation. Moreover, sample $E_{l3} - \tau_R^{min}$ is about three times more cracked than the samples $E_{l1} - \tau_R^{min}$, although it has less grain boundaries with a high misorientation angle, due to larger grains. Contrary to initial thought, the crack density is not correlated to the density of grain boundaries with a high misorientation. The reason for this is that all samples have a density of highly misorientated grain boundaries (more than 20mm/mm² with an angle over 40°) which is far larger than the crack density (less than 3mm/mm²). Only a small proportion of these grain boundaries features cracks. As a consequence, grain structure does not account for the difference between highly cracked samples and the ones without cracks.

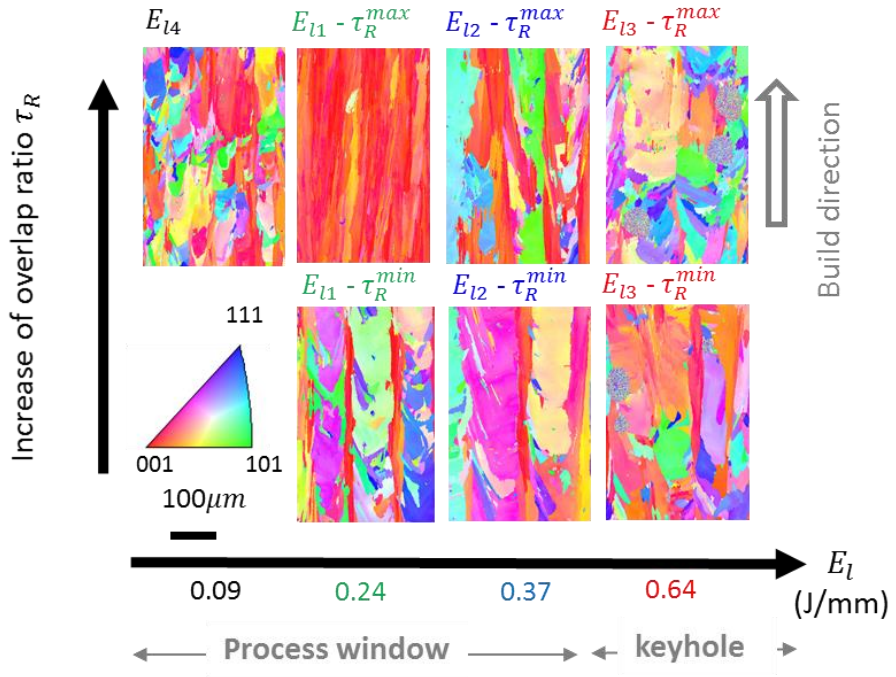

Figure 19 - Grain structure of samples with different fabrication parameters.

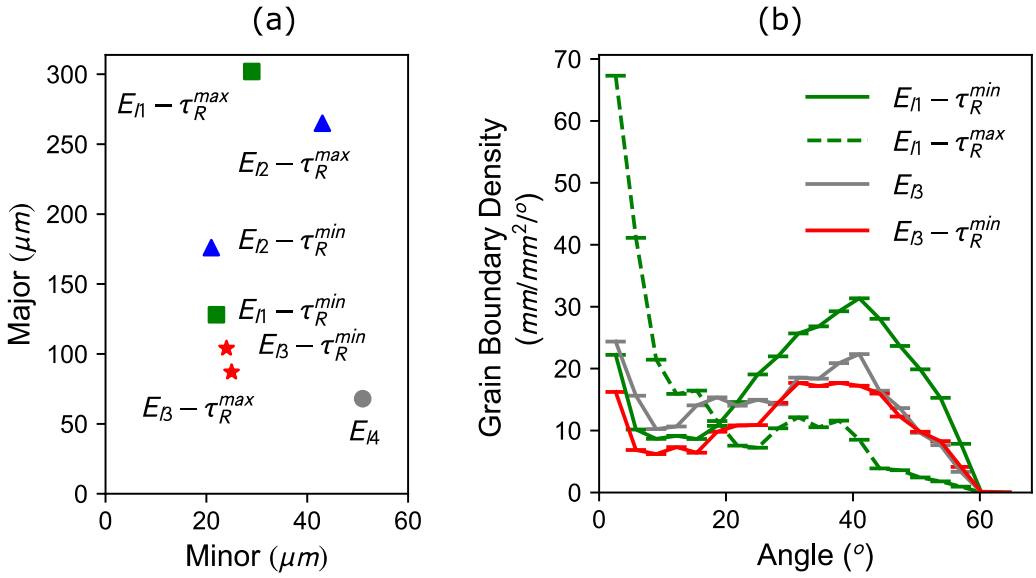

Figure 20 - Grain size of the samples (a) and grain boundary density function (b).

8.3. Mechanical stresses

In welding, solidification cracks are usually longitudinal [28]. It was observed in this study that the cracks always initiate transversally to the melt pool, which is conform to Cloots' observations [8]. As a consequence, the initiation of the cracks is caused by a tensile stress in

the direction parallel to scanning direction (longitudinal stress). According to the Rosenthal model, the temperature gradient in the mushy zone is lower for large melt pools. One cannot say that a lesser gradient in this zone means less stress in this region. Indeed, Dye, Hunziker and Reed [29] show with thermomechanical simulations of IN718 welding that the mushy zone is constrained by its surroundings and notably by the heat affected zone. Tensile stress in the mushy zone is the result of differential thermal expansion between the mushy zone and the heat-affected zone. They show that under high linear energy conditions, the contraction of the melt pool during solidification is not compensated by the expansion of the heat-affected zone, causing a tensile stress in the mushy zone. Although their study considers welding, it is compatible with our observation on the LBM process that there are more cracks when the material is processed with large melt pools.

8.4. Overlap ratio

The effect of the overlap between melt pools has not yet been written about. Depending on the fabrication conditions (low or high linear energy), Carter et al. [9] measure either an increase or a decrease of microcracking with the hatching space. In this study, a decrease of the microcracking with hatching space was observed in any cases. During the fabrication of a layer, the material which is solidified in a melt pool is then partially remelted during the fusion of the adjacent melt pool. The more overlap, the more remelting. With an observation of the upper layer, it was noticed that cracks do not propagate again in the adjacent melt pool during its solidification (Figure 11.a). As a consequence, remelting repairs partially the cracks. It can be understood with Figure 11.b that a higher overlap will induce narrower cracks. Narrow cracks

are likely to have a lower probability of propagation in higher fabrication layers, as it was observed in Figure 3. This provides a possible explanation for the effect of the overlap ratio on the cracking density.

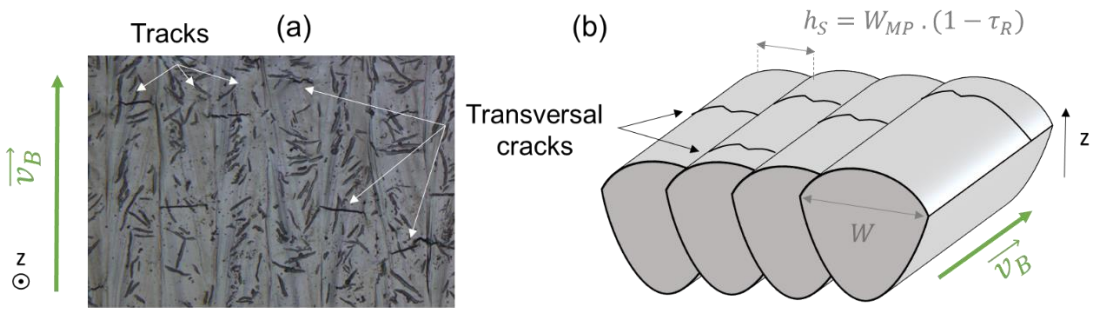

Figure 21 – Effect of overlap on crack repair : (a) cracks visible on the upper layer of a sample (top view) ; (b) partial repair of cracks remelting.

8.5. Alloy composition

To investigate the role of composition, five samples were fabricated in René 77. This superalloy has approximately the same content in γ'-forming elements: $Ti + Ta + Nb + Al$ = 13.1 at% for the René 77 (Table 1) and 13.9 at% for the IN738 LC. The two materials have therefore a similar position in common weldability diagrams [2,30]. The crack density was measured for five samples in René 77 using the same fabrication parameters as for IN738 LC. We can see on Figure 22 that René 77 has a lower susceptibility to solidification cracking than IN738 LC. As described before, a thin cut was collected in some samples and bent up to failure. The failure surface was then observed with a SEM. The crack surface of IN738 LC shows dendritic structure with microporosity between the dendrite arms. On the contrary, the failure surface of the sample of René 77 (Figure 22.b) is smooth, which suggests that the failure does not follow the dendrites interfaces as for IN738 LC. The microporosity in IN738 LC demonstrates a lack of liquid metal feeding in the last stages of solidification, which also causes a susceptibility of

this material to solidification cracking. To understand this difference, the evolution of the solid fraction f_s as a function of temperature was calculated with Thermocalc software and TCNI9 database. As in other studies [8,10,13,15] , it was considered that Gulliver-Scheil model (i.e. infinite diffusion of chemical species in the liquid phase and no diffusion in the solid phase) is the best model available to describe rapid non-equilibrium solidification, although it does not account for possible solute trapping [31,32]. Table 2 gives for the two alloys the liquidus temperature T_l, the temperature for which the solid fraction is fs=0.9 and solidus temperature T_s (assimilated to fs=0.99). Freezing range $\Delta T = T_l - T_s$ is larger for the Inconel 738 batch than for the René 77. The brittle temperature range $\Delta T_{BTR} = T(f_s = 0.9) - T(f_s = 0.99)$ estimated is 120°C for the batch of Inconel 738 and 91°C for the René 77, which explains the higher susceptibility of Inconel 738 to cracking. Let us note that the solid fraction limits of the BTR varies between authors, due to difficulties to measure it. Consequently, it was verified that ΔT_{BTR} is larger for Inconel 738, according to the other definitions found in literature, such as $0.7 < f_s < 0.98$ [29,33] or $0.95 < f_s < 1$ [13].

	T_l $(f_s = 0)$	$T(f_s = 0.9)$	T_s $(f_s = 0.99)$	ΔT	ΔT_{BTR}
Inconel 738	1340°C	1147°C	1027°C	313°C	120°C
René 77	1355°C	1216°C	1125°C	230°C	91°C

Table 2 – Gulliver-Scheil solidification calculation with Thermocalc software and TCNI9 database

There is an interest in understanding what differences in the alloy compositions (Table 1) cause the higher susceptibility to cracking of the samples in Inconel 738. On the one hand, this alloy

batch includes more Si and more Zr. Engeli et al. [7] reported a detrimental effect of Si and discussed the possible causes, among which an increase of the solidification interval. For Cloots et al. [8], segregation of Zr is the cause of an increase of solidification interval. On the other hand, the Inconel 738 batch contains also less B, which is according to Chauvet et al. [13] at the origin of a residual liquid film between grains at a low temperature, i.e. an increase of ΔT_{BTR}.

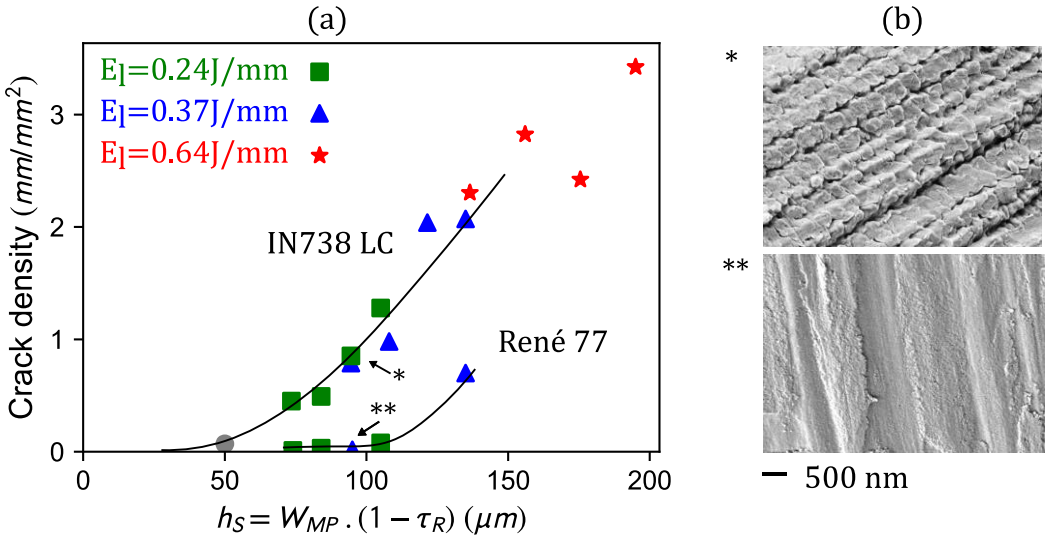

Figure 22 - (a) Difference of solidification cracking susceptibility between IN738 LC and René 77 ; (b) cracks surface of samples bend up to failure.

It is worth noting that the comparison of characteristic temperature interval (ΔT or ΔT_{BTR}) may not be sufficient to account completely for the cracking susceptibility difference between these two alloys. Lecomte-Beckers [34] studied with eight experimental superalloys the influence of six elements (C, Cr, Co, Mo, Mo, Ti, Al) on microporosity after casting. She proposes a model of the pressure drop Δp_l of the liquid metal in the mushy zone to account for a lack of liquid metal feeding:

$$\Delta p_l = \frac{v_S}{G} \times 24\mu_l \beta \tau^3 n. \Delta T \qquad \text{Equation 5}$$

where G and v_S are the thermal gradient and the solidification speed, μ_l is the viscosity, $\beta = (\rho_s - \rho_l)/\rho_l$ is the solidification shrinkage, ρ_s and ρ_l are the density of the solid phase and of the liquid phase, τ is the tortuosity of the dendritic network in the mushy zone, n is the number of interdendritic channels per unit area and ΔT is the freezing range. In addition to the effect of ΔT, Lecomte-Becker also discusses the role of some chemical elements on the tortuosity τ of the dendritic network in the mushy zone. For example, titanium increases tortuosity more than aluminum and therefore decreases the permeability of the mushy zone. A higher ratio $(Ti + Ta + Nb)/Al$ [35] for Inconel 738 LC (0.6 at% / at%) compared to René 77 (0.4 at% / at%) could then contribute to a higher tortuosity and then a lack of liquid metal feeding in the last stages of solidification. Zhang and Singer [33] describe a possible role of carbides, which solidify in the interdendritic channels and then also reduce the permeability of the mushy zone. This phenomenon is also discussed by Xu et al. [15]. Due to the higher content of C and of Nb in Inconel 738, primary (Ti, Nb)C carbides form earlier the mushy zone ($f_s = 0.37$ for Inconel 738 and $f_s = 0.68$ for René 77). It is possible that they also play a role in the cracking susceptibility difference. In fact, it is difficult with a comparison between two alloys to distinguish between the role major elements and the role of minor elements. It is very likely that the content in major elements does have a role in the difference of behavior between these two alloys, in spite of the additional effect of minor elements. This issue is the object of a current study.

9. Conclusions

The goal of this study was to link the fabrication parameters, the geometry of the melt pools and the occurrence of solidification cracking. It was shown that larger melt pools lead to more microcracking. With the same melt pool width, more overlap leads to less cracking, which was attributed to a partial repair of cracks by remelting. These findings have made possible the fabrication of a dense and crack free material, by controlling the melt pool size combined with a control of the overlap ratio. The difference in cracking density could not be explained by a difference in high-angle grain boundaries density. As all samples have enough HAGBs, the difference of cracking is thought to be a consequence of the size of the mushy zone and of the intensity of the mechanical stresses. Finally, a comparison with René 77 confirmed the importance of the freezing range and the brittle range temperature on cracking susceptibility.

Acknowledgments

Safran Tech (Châteaufort, France) funded this study.

References

[1] R.C. Reed, The Superalloys: Fundamentals and Applications, Cambridge University Press, Cambridge, 2006. doi:10.1017/CBO9780511541285.

[2] M.J. Donachie, S.J. Donachie, Superalloys: A Technical Guide, 2nd Edition, ASM International, 2002.

[3] A.T. Egbewande, H.R. Zhang, R.K. Sidhu, O.A. Ojo, Improvement in Laser Weldability of Inconel 738 Superalloy through Microstructural Modification, Metall. Mater. Trans. A. 40 (2009) 2694. doi:10.1007/s11661-009-9962-6.

[4] O.A. Ojo, N.L. Richards, M.C. Chaturvedi, Liquation of various phases in HAZ during welding of cast Inconel 738LC, Mater. Sci. Technol. 20 (2004) 1027–1034. doi:10.1179/026708304225019948.

[5] J.E. Franklin, W.F. Savage, Stress relaxation and strain-age cracking in Rene 41 weldments, Weld J N. 53 (1974) 380–387.

[6] M. Rowe, Ranking the resistance of wrought superalloys to strain-age cracking, Weld. J. 85 (2006) 27–33.

[7] R. Engeli, T. Etter, S. Hövel, K. Wegener, Processability of different IN738LC powder batches by selective laser melting, J. Mater. Process. Technol. 229 (2016) 484–491. doi:10.1016/j.jmatprotec.2015.09.046.

[8] M. Cloots, P.J. Uggowitzer, K. Wegener, Investigations on the microstructure and crack formation of IN738LC samples processed by selective laser melting using Gaussian and doughnut profiles, Mater. Des. 89 (2016) 770–784.

[9] L.N. Carter, M.M. Attallah, R.C. Reed, Laser powder bed fabrication of nickel-base superalloys: influence of parameters; characterisation, quantification and mitigation of cracking, in: Proc 12th Int Symp Superalloys Champion PA 9–13 Sept. 2012, 2012: pp. 577–586.

[10] D. Tomus, P.A. Rometsch, M. Heilmaier, X. Wu, Effect of minor alloying elements on crack-formation characteristics of Hastelloy-X manufactured by selective laser melting, Addit. Manuf. 16 (2017) 65–72. doi:10.1016/j.addma.2017.05.006.

[11] N.J. Harrison, I. Todd, K. Mumtaz, Reduction of micro-cracking in nickel superalloys processed by Selective Laser Melting: A fundamental alloy design approach, Acta Mater. 94 (2015) 59–68. doi:10.1016/j.actamat.2015.04.035.

[12] K. Kunze, T. Etter, J. Grässlin, V. Shklover, Texture, anisotropy in microstructure and mechanical properties of IN738LC alloy processed by selective laser melting (SLM), Mater. Sci. Eng. A. 620 (2015) 213–222. doi:10.1016/j.msea.2014.10.003.

[13] E. Chauvet, P. Kontis, E.A. Jägle, B. Gault, D. Raabe, C. Tassin, J.-J. Blandin, R. Dendievel, B. Vayre, S. Abed, G. Martin, Hot cracking mechanism affecting a non-weldable Ni-based superalloy produced by selective electron Beam Melting, Acta Mater. 142 (2018) 82–94. doi:10.1016/j.actamat.2017.09.047.

[14] M. Gäumann, C. Bezençon, P. Canalis, W. Kurz, Single-crystal laser deposition of superalloys: processing–microstructure maps, Acta Mater. 49 (2001) 1051–1062. doi:10.1016/S1359-6454(00)00367-0.

[15] J. Xu, X. Lin, P. Guo, H. Dong, X. Wen, Q. Li, L. Xue, W. Huang, The initiation and propagation mechanism of the overlapping zone cracking during laser solid forming of IN-738LC superalloy, J. Alloys Compd. 749 (2018) 859–870. doi:10.1016/j.jallcom.2018.03.366.

[16] I. Yadroitsev, P. Krakhmalev, I. Yadroitsava, S. Johansson, I. Smurov, Energy input effect on morphology and microstructure of selective laser melting single track from metallic powder, J. Mater. Process. Technol. 213 (2013) 606–613. doi:10.1016/j.jmatprotec.2012.11.014.

[17] H. Gu, H. Gong, D. Pal, K. Rafi, T. Starr, B. Stucker, Influences of energy density on porosity and microstructure of selective laser melted 17-4PH stainless steel, in: 2013 Solid Free. Fabr. Symp., 2013.

[18] K. Darvish, Z.W. Chen, T. Pasang, Reducing lack of fusion during selective laser melting of CoCrMo alloy: Effect of laser power on geometrical features of tracks, Mater. Des. 112 (2016) 357–366. doi:10.1016/j.matdes.2016.09.086.

[19] W.E. King, H.D. Barth, V.M. Castillo, G.F. Gallegos, J.W. Gibbs, D.E. Hahn, C. Kamath, A.M. Rubenchik, Observation of keyhole-mode laser melting in laser powder-bed fusion

additive manufacturing, J. Mater. Process. Technol. 214 (2014) 2915–2925. doi:10.1016/j.jmatprotec.2014.06.005.
[20] I. Yadroitsev, I. Smurov, Surface Morphology in Selective Laser Melting of Metal Powders, Phys. Procedia. 12 (2011) 264–270. doi:10.1016/j.phpro.2011.03.034.
[21] O.M.D.M. Messé, R. Muñoz-Moreno, T. Illston, S. Baker, H.J. Stone, Metastable carbides and their impact on recrystallisation in IN738LC processed by selective laser melting, Addit. Manuf. 22 (2018) 394–404. doi:10.1016/j.addma.2018.05.030.
[22] J.A. Dantzig, M. Rappaz, Deformation during solidification and hot tearing, in: Solidification, EPFL press, 2009.
[23] T. Clyne, G. Davies, Influence of composition on solidification cracking susceptibility in binary alloy systems, 74 65–73.
[24] D. Rosenthal, The theory of moving sources of heat and its application of metal treatments, Trans. ASME. 68 (1946) 849–866.
[25] L. Thijs, K. Kempen, J.-P. Kruth, J. Van Humbeeck, Fine-structured aluminium products with controllable texture by selective laser melting of pre-alloyed AlSi10Mg powder, Acta Mater. 61 (2013) 1809–1819. doi:10.1016/j.actamat.2012.11.052.
[26] N. Wang, S. Mokadem, M. Rappaz, W. Kurz, Solidification cracking of superalloy single- and bi-crystals, Acta Mater. 52 (2004) 3173–3182. doi:10.1016/j.actamat.2004.03.047.
[27] M. Rappaz, A. Jacot, W.J. Boettinger, Last-stage solidification of alloys: Theoretical model of dendrite-arm and grain coalescence, Metall. Mater. Trans. A. 34 (2003) 467–479. doi:10.1007/s11661-003-0083-3.
[28] T. Böllinghaus, H. Herold, C.E. Cross, J.C. Lippold, eds., Hot Cracking Phenomena in Welds II, Springer Berlin Heidelberg, Berlin, Heidelberg, 2008. doi:10.1007/978-3-540-78628-3.
[29] D. Dye, O. Hunziker, R.C. Reed, Numerical analysis of the weldability of superalloys, Acta Mater. 49 (2001) 683–697. doi:10.1016/S1359-6454(00)00361-X.
[30] M. Rowe, Ranking the resistance of wrought superalloys to strain-age cracking, Weld. J. 85 (2006) 27s–33s.
[31] J.V. Wood, P.F. Mills, A.R. Waugh, J.V. Bee, Rapidly solidified nickel-base superalloys, J. Mater. Sci. 15 (1980) 2709–2719. doi:10.1007/BF00550537.
[32] L. Liu, F. Sommer, H.Z. Fu, Effect of solidification conditions on MC carbides in a nickel-base superalloy IN 738 LC, Scr. Metall. Mater. 30 (1994) 587–591. doi:10.1016/0956-716X(94)90434-0.
[33] J. Zhang, R.F. Singer, Hot tearing of nickel-based superalloys during directional solidification, Acta Mater. 50 (2002) 1869–1879. doi:10.1016/S1359-6454(02)00042-3.
[34] J. Lecomte-Beckers, Study of microporosity formation in nickel-base superalloys, Metall. Trans. A. 19 (1988) 2341–2348.
[35] J. Guédou, I. Augustins-Lecallier, L. Nazé, P. Caron, D. Locq, Development of a new fatigue and creep resistant PM nickel-base superalloy for disk applications, in: Proc. Elev. Int. Symp. Superalloys, 2008: pp. 21–30.

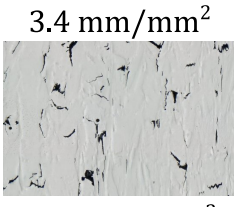
3.4 mm/mm²
0.07mm/mm²
500 µm

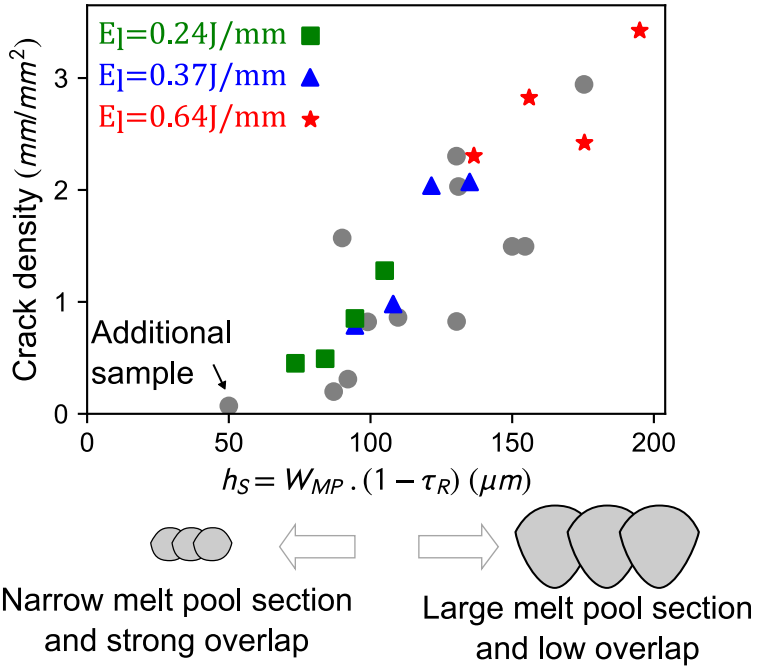
E_l=0.24J/mm
E_l=0.37J/mm
E_l=0.64J/mm
Crack density (mm/mm²)
Additional sample
0
1
2
3
0
50
100
150
200
h_S = W_MP . (1 − τ_R) (µm)
Narrow melt pool section and strong overlap
Large melt pool section and low overlap